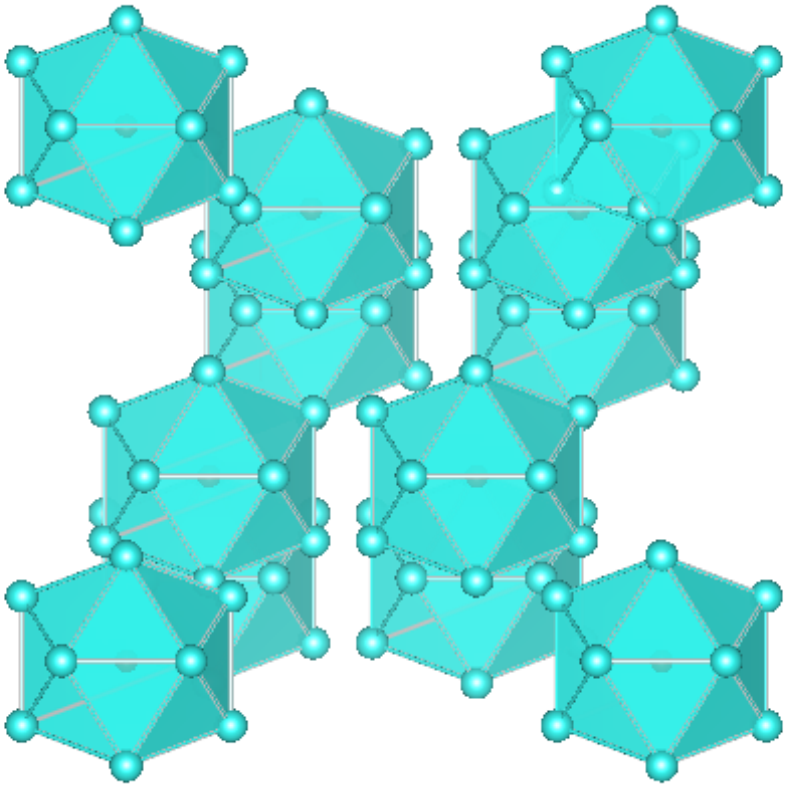
Structure Determination of the (111) Surface of the 2/1 Ag-In-Yb Quasicrystal Approximant



A thesis submitted in partial fulfillment of the requirements for the degree of Master of Physics

Matthew Barton (201861015)

Supervised by: Dr Hem Raj Sharma

UNIVERSITY OF LIVERPOOL

Declaration of Authorship

I, Matthew Barton, declare that the thesis entitled 'Structure Determination of the (111) Surface of the 2/1 Ag-In-Yb Quasicrystal Approximant' and the work presented in it are my own. I confirm that:

- This work was done wholly or mainly while in candidature for a research degree at this University.
- Where any part of this thesis has previously been submitted for a degree or any other qualification at this University or any other institution, this has been clearly stated.
- Where I have consulted the published work of others, this is always clearly attributed.
- Where I have quoted from the work of others, the source is always given. With the exception of such quotations, this thesis is entirely my own work.
- I have acknowledged all main sources of help. Where the thesis is based on work done by myself jointly with others, I have made clear exactly what was done by others and what I have contributed myself.

Contents

Declaration of Authorship v

Acknowledgements v

Abstract vi

1 Introduction 1

2 Background Theory 2

2.1 Elementary Crystallography . . . 2

2.1.1 Crystal Basis . . . 2

2.1.2 Miller Indices . . . 2

2.2 Surface Science . . . 3

2.2.1 Reconstruction and Relaxation . . . 3

2.2.2 Defects . . . 4

2.3 Quasicrystals & their approximants . . . 4

2.3.1 Quasicrystals . . . 4

2.3.2 Approximants . . . 5

2.4 2/1 Ag-In-Yb Approximant . . . 5

3 Methodology 6

3.1 Ultra-High Vacuum (UHV) Chambers . . . 7

3.2 STM Methods and Analysis . . . 7

3.2.1 STM Theory . . . 7

3.2.2 Sample Preparation . . . 9

3.2.3 Analysis Procedure . . . 9

3.3 LEIS Methods and Analysis . . . 10

3.3.1 LEIS Theory . . . 10

3.3.2 Experimental Procedure . . . 10

3.3.3 Spectra Analysis Method . . . 11

3.4 Vesta and STM Simulation Methods . . . 11

3.4.1 Vesta Modelling . . . 11

3.4.2 Computational Comparisons . . . 12

4 Results and Analysis 13

4.1 STM Analysis . . . 13

4.1.1 Observed Stepheights . . . 13

4.1.2 Theoretical Bulk Stepheights . . . 14

4.1.3 STM motifs . . . 14

4.1.4 Theoretical Surface motifs . . . 15
4.1.5 Computational STM motifs . . . 16
4.2 LEIS Analysis . . . 18
4.2.1 Composition Matching . . . 19

5 Discussion of Surface Stabilities 20
5.1 Model Overview . . . 20
5.2 Chemical Stability Analysis . . . 21
5.2.1 Areal Density Studies . . . 21
5.2.2 Cluster Centre Analysis . . . 23
5.2.3 Glue Atoms . . . 24
5.2.4 Screw Defects . . . 25

6 Conclusions and Further Work 25

Bibliography vi

List of Figures xi

List of Tables xi

7 Appendices xi
7.1 Fibonacci Sequence . . . xii
7.2 Structure Visualisation . . . xii
7.3 Appendix A - STM Data Processing and Measurement Methods . . . xiii
7.3.1 STM Image Processing . . . xiii
7.3.2 Motif Measurements . . . xv
7.3.3 Step-Height Measurement . . . xviii
7.3.4 Variation in A/B motif ordering . . . xx
7.4 Appendix B - Step Height Analysis and Gaussian Fitting . . . xxii
7.4.1 Bin Fitting . . . xxii
7.4.2 Chi-squared Analysis . . . xxiii
7.4.3 Histogram Uncertainty . . . xxv
7.5 Appendix C - LEIS Spectra Analysis . . . xxvi
7.5.1 LEIS Spectra fitting . . . xxvi
7.5.2 Composition Extraction . . . xxx
7.5.3 Additional C2 Composition . . . xxxviii
7.6 Appendix D - Computational STM Model and Code Repository . . . xxxviii
7.6.1 Code Repository . . . xxxviii
7.6.2 Brief Model Overview . . . xxxix
7.6.3 Model Implementation . . . xxxix

7.6.4 Model Limitations xl
7.6.5 Additional Data xli
7.7 Appendix E - VESTA Analysis xliii
7.7.1 Analysis an Example xliii
7.7.2 Motif Measurements xlvi
7.8 Appendix F - Required Materials xlvi
7.8.1 AI summary xlvi
7.8.2 Copy of Project Plan xlvi
7.8.3 Introduction xlvi
7.8.4 Methods xlvii
7.8.5 Planned Work xlviii
7.8.6 References xlix
7.8.7 Lay Summary xlix
7.8.8 Overview of Contributions from others lii

Acknowledgements

I would like to thank my supervisor Dr Sharma for being incredibly supportive throughout the process, providing me with invaluable insight and experience during the many occasions in which I hit a dead end or became stuck. Additionally, I'd like to acknowledge the effort he personally went to in order to adapt supervision to suit online study during the period in which I was cast bound and unable to attend in person appointments. The success of the project would not have been possible without his excellent supervision and it would be remiss of me not to fully acknowledge it.

I would also very much like to thank Dr Coates for his expertise and support including: coming up with the layer convolution hypothesis used to describe plane A and B. Furthermore, for providing the cleaned STM data which comprises the majority of the report, constructing the initial Vesta model of the bulk and writing the base form of the STM computational model code with which so much progress was able to be made. All of which performed under no obligation and alongside a very busy teaching and research schedule.

Finally, I would like to thank Dr Gardner for running LEIS experimentation with me. Not only working quite literally day and night for 2 days to provide me with the 3 sputtering cycles needed but also providing invaluable help in understanding LEIS and performing the experimental analysis.

Abstract

The primary aim of this project is to describe the surface formation of the previously unstudied 2/1 Ag-In-Yb approximant along the (111) plane direction. These approximants often offer invaluable insight into their more complex quasicrystal parent, fuelling the development of valuable material technologies from catalysts to photovoltaics.

Using low-energy ion spectroscopy (LEIS) methods combined with scanning tunnelling microscopy (STM) imaging, we successfully developed an understanding of the species present on the surface and the planes along which the surface terminates. From this experimental analysis, we identified that the surface formed along 3 Yb-rich subplanes (A, B and C), demonstrating additional fragmentation of the surface into smaller metastable subplanes. This conclusion was strengthened by the use of step-height analysis, which demonstrated 4 distinct step-heights, including a smaller 0.8 Å - 1.1 Å step. This indicated the presence of divides between adjacent subplanes. Additional use of a computational STM model permitted matching of our observed STM motifs to specific arrangements of species on our theoretical subplanes, strongly indicating their presence.

Finally, chemical analysis techniques, such as areal density methods, were employed. These demonstrated that plane stability is determined by a mixture of: Yb density, minimisation of destabilising cleavage of Tsai clusters and finally the stabilisation of low density subplanes by relaxation into neighbouring In-rich planes with lower surface free energy. This analysis supported the presence of our subplanes, indicating them to be highly stable compared to other possible surface terminations. Furthermore, this partially refuted the hypothesis that the structure terminates solely along Tsai cluster-centre planes similar to the previously studied 1/1 approximant. Instead, indicating the importance of other chemical stability features, such as In support, giving our approximant a much more varied and stochastic surface profile.

Our model, although successfully implemented on our available dataset, does require further work to consolidate. We recommend X-ray Photoelectron Spectroscopy studies (XPS) to help eliminate the influence of LEIS uncertainty and possible In migration models. Additionally, a larger STM data set would be beneficial in reducing overall uncertainty. Additionally, our work may provide impetus for further studies on 2/1 or coarser approximants with the stochastic surface profile having possible novel adsorption or electronic properties.

1 Introduction

First discovered in 1982 by Dan Schectman, quasicrystals have spawned a wave of excitement amongst the solid state community, culminating in the award of the 2011 Nobel prize in Chemistry to Schectman for their discovery [1]. What makes these crystals so revolutionary is that they disobey the time-tested foundational law of crystal structure, having no periodic structure at all. Up until their discovery, it was believed that all crystals must show a periodic structure, with non-periodic structures only being observed in mixed solids and soft matter materials [2]. However, unlike normal crystals, which are neatly periodic, quasicrystals show a mixture of structures which never repeat yet still form a cohesive crystal. Additionally, quasicrystals demonstrate a property known as long-range order; this effectively means that they can be reconstructed from a limited number of base structures (ie Tsai Clusters) repeated uniquely throughout space. Crucially, this property means that quasicrystals show ordered diffraction patterns with bright diffraction spots. This has made the study and characterisation of quasicrystals much more feasible, opening the doors to many exciting applications [3].

Principally, quasicrystals present an interesting number of mathematical applications. Primarily, their aperiodicity, which can be described mathematically using aperiodic functions. These functions extend to describe the famous tiling problems in which an infinite plane must be tiled by regular polyhedra [4]. For instance, our Ag-In-Yb quasicrystal, from which our approximant is derived, can be characterised using the famous Penrose pentagonal tiling [5]. Additional mathematical avenues of interest arise via the self-similarity of quasicrystals; being composed of repeating units with varying orientations, they closely resemble fractal patterns like the Sierpinski triangles [6]. This similarity may open new avenues in characterising the mathematical features of the quasicrystal surfaces [7].

Furthermore, more practical applications of quasicrystals may revolutionise material science, providing solutions to a number of open problems. These range from replacing harmful Teflon in non-stick pans to reinforcing steel to make super-tensile strength structures [8]. Importantly for industry, quasicrystals can also be deployed as catalysts within various chemical reactions. Their non-repeating structure allows the identification of numerous high-density surfaces onto which adsorption can occur. This means quasicrystals may one day open the door to cheaper catalysis of common reactions like the steam reformation of methanol [9].

The study of quasicrystals is unfortunately highly complicated due to their non-periodic nature. This makes resolving and studying their structure highly complex. Luckily, all aperiodic functions from which quasicrystals can be derived can also be approximated. For quasicrystals, this takes the form of approximants which locally resemble the quasicrystal but have a repeating unit cell structure. This renders them significantly easier to study by conventional

techniques while also providing invaluable insight into the local structure of the quasicrystal [10]. Specifically, within this project, we focused on the 2/1 Ag-In-Yb approximant with the aim of describing the structure of its (111) surface. This should assist in the study of its corresponding quasicrystal, which provides invaluable insight into general icosahedral quasicrystals thanks to its well-structured nature and relative stability [11]. In addition, studies on 2/1 or finer approximants have never been attempted for any quasicrystal system; consequently, we hope our study may bridge a vital gap in our structural understanding of higher order approximant surfaces and their relation to their quasicrystal parent systems.

2 Background Theory

This section aims to familiarise the reader with the many basic crystallographic and surface science concepts used throughout this thesis. This section may be skipped by readers familiar with quasicrystals and general crystallography.

2.1 Elementary Crystallography

2.1.1 Crystal Basis

Conventional crystals are periodic atomic structures. This means that they are composed of a small base units (unit cells) which can be tessellated to construct the entire crystal structure. We can describe the crystal mathematically using a lattice. This is a mathematical basis of $\mathbb{R}^3$ constructed using the crystal structure as a reference. We first define 3 vectors known as the crystal vectors that span $\mathbb{R}^3$:

$$R = a\hat{\imath} + b\hat{\jmath} + c\hat{k} \tag{1}$$

Where R is the vector distance between our chosen lattices points, i, j, k are the lattice vectors, and a, b, c are real numbers. We may use these vectors to derive the position of any lattice point. Then, on top of these lattice points, we can specify an atomic basis which ascribes to each point in our lattice a specific atomic species. Consequently, using this atomic basis and our lattice we can predict both the atom species present and location of all atoms within our crystal, providing us with a mathematical description of the holistic crystal structure as well as its various symmetries [12].

2.1.2 Miller Indices

It is often useful to be able to identify specific planes of atoms within the crystal. This is especially pertinent to our project, as our surface forms along a specific plane of atoms: the (111) plane. We may delineate these planes using Miller indices [13]. We derive these indices

by taking the axis intercepts of our chosen plane. We then take their reciprocal and reduce these reciprocal values to the lowest common set of integers with the same ratio. An illustrative example can be seen in the figure below:

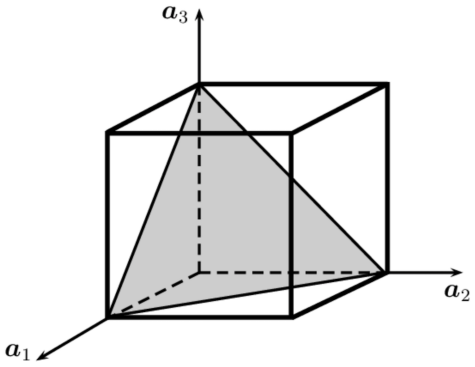


Figure 1: Example of a (111) plane over-layed onto cubic unit cell with basis vectors a_i. The x, y and z intercepts are all at unity relative to the lattice vectors hence taking their reciprocal and finding the integer ratio we get (111) as our Miller indices. [Kittel [13]]

2.2 Surface Science

Being able to describe the bulk crystal structure is often insufficient for fully describing the crystal surface. Various potential minimising effects often mean that the surface structure is distinct from that of the bulk [14]. The overall surface structure is composed of various flat planes of atoms and drops between them. These flat planes are known as terraces, with drops being known as step defects. These terraces form along the most energetically favourable plane of atoms. For instance, a surface cut along the (111) plane direction may demonstrate steps between planes of higher atomic density or coordination number [15]. As a result, we never see a perfectly flat surface, but rather, a series of separated, energetically favourable terraces.

2.2.1 Reconstruction and Relaxation

At the surface, the bond coordination number of each atom is less than that within the bulk structure. This lack of coordination leads to a higher energy at the surface. This is due to a net force pulling the surface layer towards the inner structure. The structure adapts to minimise this net potential in a number of ways; the two most common are surface reconstruction and relaxation [16]:

Relaxation is a process by which the top planes of atoms relax towards the bulk. This reduces the overall surface energy at the top layer, leading to a more stable surface structure. The first plane relaxes towards the second. The third plane then moves further away from the second due to this relaxation, and so on. Hence, we see an oscillation of plane separations for the first few layers. Meanwhile, reconstruction is the process whereby the surface structure changes to

minimise the potential. This may consist of certain atomic species being drawn further together or apart, forming new covalent bonds to increase their coordination number. This, in contrast to relaxation, leads to a fundamental change in the surface structure and its symmetry [17].

2.2.2 Defects

Surface structures often demonstrate defects or imperfections. These can include the addition of atoms on top of the terrace, kinks in the terrace line, and atomic vacancies. Additionally, less common defects can also arise during the preparation of the sample. One defect of particular note within our project was screw dislocations. These are helical distortions in the crystal surface usually caused by shearing of crystal planes during the cutting process [18].

2.3 Quasicrystals & their approximants

2.3.1 Quasicrystals

There exist only certain allowed symmetry groups within crystals due to the crystal restriction theorem. This requires that unit cells tessellate, forming a 3D periodic structure without gaps [19]. For example, pentagonal prisms, as mentioned within the introduction, are forbidden and thus, so is 5-fold symmetry [20].

Quasicrystals are formed by these forbidden structures. Consequently, they show no periodicity within their holistic structure. Crucially, however, quasicrystals do demonstrate 'long-range' order. This means that their structure can be spanned by rows of atoms, which maintain their orientation. Therefore, despite no periodic structure being present, quasicrystals demonstrate bright diffraction patterns [21].

We may describe the quasicrystal mathematically using almost periodic functions. These are functions having no set period but an arbitrary number of 'almost' repeats. Importantly, these almost periodic functions can be constructed by using higher-dimensional periodic functions. For quasicrystals, this is done using the cut and project method. Effectively, a higher-dimensional periodic lattice is decomposed into 2 orthogonal subspaces $E_{||}$ and $E_{\perp}$. We choose $E_{||}$ such that it is irrationally oriented relative to the higher-dimensional lattice. For each lattice point, we decompose its position into components in $E_{||}$ and $E_{\perp}$. If the perpendicular component lies inside a bounded region $W \subset E_{\perp}$, we keep the point and use its projection onto $E_{||}$ as an atomic position. This construction yields an aperiodic point set. This point set is our quasicrystal lattice [22].

For example, within Figure 2, we take a 2D point space and draw a dividing line through it with a certain slope. We then project points from a chosen area W onto our slope, creating

a 1D lattice. Additionally, if we chose that slope to be an irrational one, our two 1D subspaces become irrationally orientated hence, we recover an aperiodic 1D lattice after projection.

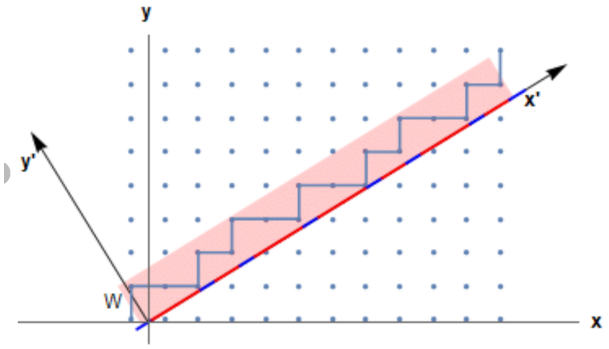


Figure 2: 2d illustration of the cut and project method our orthogonal subset is to be the line y=mx with the projection region W highlighted in orange. [A.Jagannathan, 2020

2.3.2 Approximants

Just as a quasiperiodic function arises as the result of an irrationally oriented $E_{||}$, rational orientations give rise to periodic functions. If we return to the 2D lattice example, take, for instance, the irrational slope τ (golden ratio), this slope can be approximated using quotients of consecutive terms in the Fibonacci sequence (see Appendix A). For instance, $\tau > \frac{1}{1}$, $\tau > \frac{2}{1}$ iterating to equality. Hence, we limit towards an aperiodic 1D crystal lattice as our slope approximation increases in accuracy. Generalising this logic to 3D quasicrystals, we can take a rationally oriented $E_{||}$ with basis vector ratios following the Fibonacci approximation of τ. This gives a periodic lattice. As we change the ratios from 1/1 to 2/1 and so forth, we eventually reconstruct the quasicrystal. Using these rational approximations, we can construct a quasicrystal approximant which has a locally similar structure to the quasicrystal but is periodic. These are known as approximants to the quasicrystal [22].

2.4 2/1 Ag-In-Yb Approximant

The 2/1 approximant is distinguished from the previously studied 1/1 approximant by a single τ scaling of the unit cell [23]. Crucially for our study, the Ag-In-Yb intermetallic quasicrystal is well-studied along with its isostructural counterpart i-Cd-Yb [24]. All approximants and quasicrystals within this intermetallic regime are characterised by their cluster composition. There exist three separate cluster types, Mackay, Bergman and Tsai. Cd/Ag-In structures are composed of Tsai clusters. These clusters are formed by 5 separate shells of atoms with varying ratios of Ag-In within the first, second, fourth and fifth shells. The third shell is composed of the rare earth atom, which is Yb in our structure [25], [26].

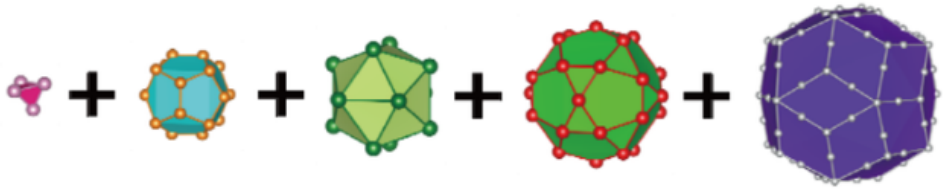


Figure 3: Decomposed Tsai cluster showing the progression of shells from smallest to largest. Third shell is composed of Yb. [S.Coates, 2019]

Focusing on our 2/1 approximant, the unit cell contains 9 clusters, one cluster centred at each vertex of the unit cell, contributing $\frac{1}{8}$ of a cluster and 8 internal clusters arranged into a two-layered diamond pattern. The actual existence of these clusters is more a helpful guide to characterising the structure than a physical rule, as in-between the clusters, there exist Yb 'glue' atoms. These glue atoms stabilise the bulk structure [27]. Dividing the unit cell into planes along the (111) direction, these clusters manifest as 3 large planes of Yb (A, B, C). These can then be further decomposed into 10 individual atomic layers of Yb atoms. These atomic planes are of particular interest due them being coplanar with the location of cluster centres (see figure 5). The location cluster-centres has previously been tightly correlated with the location of plane terminations within the 1/1 Au-Al-Tb and 1/1 Ag-In-Yb cubic approximants [24][28].

3 Methodology

In this section a brief overview of the methods used will be presented. This will include: the basic theory and use of experimental apparatus, as well as, a discussion of data collection and preparation methods used.

3.1 Ultra-High Vacuum (UHV) Chambers

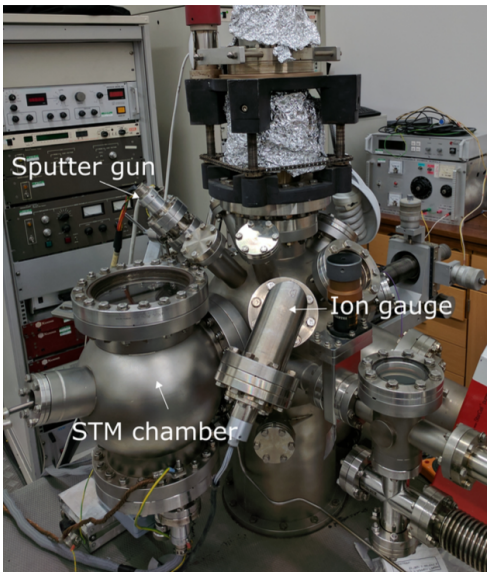


Figure 4: Diagram of the STM UHV chamber contained within the SSRC lab. [Sam Coates, 2019]

All experiments were performed under UHV conditions to minimise the presence of contaminants such as hydrocarbons. Like any reactive metal sample, we expect oxidation to occur under atmospheric conditions, with translocation of species dependent on oxide stability [29]. The combination of oxidation and translocation invariably renders the surface completely dissimilar to the structure of the uncontaminated sample and thus must be minimised by preparation of the sample under UHV conditions.

Due to the extreme sensitivity of our surface to the presence of surface and atmospheric contaminants, pressures of 10^{-11} mbar must be employed when conducting STM (see section 3.2.1) analysis. This requires the use of three separate pumps in tandem: a roughing pump (Rotary Vane within our set-up), a turbo-molecular pump and an ion pump [30].

For Leis (see section 3.3.1) analysis, due to repeated sputtering, removing contaminants before build-up, much lower pressures of around 10^{-8} mbar are needed. Thus, only a roughing and turbo-molecular pump were used [31].

3.2 STM Methods and Analysis

3.2.1 STM Theory

Our STM apparatus consisted of a tungsten scanning tip driven by small piezoelectric drives. Our tip was, in turn, connected to a voltage supply to allow application of a bias voltage. Additionally, a signal amplifier was connected to the tip to allow recording of the tunnelling current

[32].

The exact theory of STM is complex and beyond the scope of this analysis. However, a small summary is needed to explain tip resolution and bias effects. Superficially, STM can be reduced to a finite square well. Effectively, we have the sample state Ψ_T, the tip state Ψ_S and then the vacuum (finite square well) between them. One of the core tenets of this finite square well is that states may tunnel through the potential well. Consequently, we observe a tunnelling of electrons across our vacuum gap. The principal assumption made by Bardeen was to then treat these tunnelling states as orthogonal (weakly coupled) and to assume they don't represent states of the overall coupled Hamiltonian. This allows us to apply basic perturbation theory using Fermi's golden rule to derive the tunnelling probabilities for each state [38]. Additionally, in real materials, there exist thousands of states in both the tip and sample, so we must also take this into account using the Fermi-Dirac distribution.

Normally, for every state in the tip, there is a corresponding occupied state of similar energy in the sample. This means that the net movement of electrons is zero. However, if a bias voltage (V) is applied between the tip and the sample, the states in the tip shift by eV relative to the Fermi level. For a positive bias, this means that occupied states now above the Fermi level in the tip can tunnel into the unoccupied states in the sample. This creates a net current from the tip to the sample, which takes the form:

$$I = \frac{4\pi e}{\hbar} V n_s n_t (E_F^t)(E_F^s)|M|^2 \tag{2}$$

Where e is the electron charge, V is the bias voltage, n_s is our sample density of states (DOS), n_t is the tip DOS, E_F^s/E_F^t is the Fermi energy of sample/tip, and M is the tunnelling matrix element. Crucially, we see that the tunnelling current is related to the LDOS (n_s) in the sample. Hence, by measuring the variation in tunnelling current, we may build an image of the LDOS at the sample surface. Furthermore, the tunnelling current is highly distance sensitive, with the tunnelling coefficient decaying exponentially with distance. Hence, if we hold our tip in constant current mode, we can measure variations in surface topography with sudden shifts in surface height leading to a measured change in current. Consequently, STM images show us the surface topography and LDOS at the sample surface [32][33][34].

We do require knowledge of the tip density of states (n_T) to derive that of the sample, with the overall state being the convolution of the sample and tip states [33]. The most commonly used model for direct calculation is that of Chen, which models contributions from various tip orbitals as derivatives of the tip wave function [35]. For our purposes, the conclusion of this model is simply that the narrower the tip, the greater the resolution due to a smaller number of contributing states. Moreover, the use of tungsten as a tip material arises due to its strong d_{z^2} state dominating the tunnelling current. This allows easy analysis under the assumption that

this is the only contributing state. Thus, our resolution is primarily dominated by tip geometry and the orbital makeup of the atom present at the tip apex [36].

3.2.2 Sample Preparation

In order for STM analysis to be conducted, the sample must be cleaned of all contaminants. These contaminants may shadow the true LDOS contributions. For our crystal, this was done using a 3-step process. First, the sample was polished manually using diamond paste and then cleaned using methanol to remove soluble impurities as well as leftover paste residue. Next, the sample was sputtered within a vacuum chamber by bombarding the surface with Ar^+ ions. These ions displace the surface species of the sample, removing the thin oxide layer and leaving behind a rough surface. Finally, the sample was annealed by heating it to 400^oC. This allowed the surface to stabilise into the most energetically favourable configuration by granting surface species sufficient thermal energy to migrate and relax [37][38].

3.2.3 Analysis Procedure

Once the sample had been prepared and mounted, we took approximately 130 images of the sample surface. Taking 9 large-scale images, with the rest being small-scale images of 150nmx150nm surface sections.

These images were then loaded into our analysis software (WSxM) [39]. For the large-scale images, step-height analysis was conducted. To do this, we first magnified a thin strip of the image showing visual terraces. Next, we used the height histogram feature to measure the distribution of heights across the surface. For a single step, this produced two Poisson curves with means separated by our step-height. This process was then repeated for various sections with different orientations and locations to account for random error. A more explicit overview of this procedure is presented in Appendix A.

From the small-scale images, we measured motif sizes and orientations. To do this, we employed the line profile feature to measure the distance between multiple rows of atoms within a motif array. By dividing this distance by the number of atoms present, the mean distance between atoms for that motif was then derived. We measured orientations and internal angles using vector calculations. Effectively, we took the cross product, which, along with our known atomic separations, allowed us to derive the sine of the internal angle. Orientations were also done more visually by importing the images into the program Inkscape. Within Inkscape, we performed various rotations on specific image sections to gauge the rough alignment between similar and dissimilar motifs across the images. All of the above methods were repeated at multiple locations across the images to increase the reliability and minimise uncertainty.

3.3 LEIS Methods and Analysis

3.3.1 LEIS Theory

LEIS works by first ionising Ne atoms by bombarding them with high velocity electrons. The ions are then accelerated to a kinetic energy of 5keV (for our apparatus) using a series of negatively charged plates and concentrated using a collimating lens. These ions are then fired towards the sample and scatter off the species present on the surface. A thin detector band then measures the kinetic energy of ions scattered at an angle of between $45 - 46^o$. As ions impact the surface and scatter elastically, they transfer a certain proportion of their kinetic energy. This energy loss is proportional to both the ion mass and the particle mass from which it scatters:

$$E_f = E_0 \left(\frac{cos(\theta) \pm \sqrt{m_a^2 - m_i^2 sin^2(\theta)}}{m_i + m_a} \right) \tag{3}$$

Where E_f is the final ion energy, m_a is the atom mass, m_i is the ion mass, and E_0 is the initial ion energy [40]. Hence, by measuring the scattered ion energy for a specific scattering angle, we can determine the species from which it scattered. Additionally, if the interaction cross sections are known, the actual surface composition can be reconstructed from the scattering spectra [41]. To do this, we must also consider the neutralisation coefficient. This quantifies the number of ions neutralised by collision either with small amounts of atmospheric contaminants or by collision with a specific species at the sample surface [42]. It is this neutralisation coefficient which renders LEIS extremely effective at surface analysis, with the high neutralisation probability of noble ions limiting contribution from layers below approximately 10nm [43]. Consequently, if we know the scattering and neutralisation cross sections, we can, with high accuracy, determine the composition of the first few atomic layers [42].

3.3.2 Experimental Procedure

For our LEIS analysis, we first affixed our sample to a sample plate. We then connected a thermocouple to monitor the surface temperature during annealing. Next, we inserted the sample into the UHV chamber. Within the chamber, we conducted a series of 3 sputtering cycles. We did this by dosing the surface with Ar^+ ions in known increments, then taking a LEIS spectrum after each dose. The first sputtering cycle was performed on the contaminated sample and was conducted to remove any trace oxides or hydrocarbons. After this cycle, the sample was annealed at 400^oC for 2 hours to allow the sputtered surface to reform. After an hour of cooling, the sample was then sputtered again, with spectra being recorded.

Afterwards, a final annealing and sputtering cycle was completed on the sample to account for possible contaminants or random surface anomalies in the initial cycle. Finally, we conducted a He^+ scattering analysis of the sample in which we took a spectrum using He^+ ions rather than Ne^+. The smaller size of He^+ allows interaction with smaller contaminant atoms such

as oxygen or carbon whose cross sections are too small to interact with Ne^+ significantly [42]. From this isolated spectra no C or O peaks were identified signalling that likely no contaminant shadowing occurred for either clean sputtering cycles.

3.3.3 Spectra Analysis Method

For each LEIS spectrum, 3 Gaussians were fitted using IONFIT, giving the distribution of ion counts for each species. The Gaussian baselines were then manually adjusted so that they all matched to account for energy dependence in the baseline counts. The curves were then integrated to give the total counts from each species.

The raw counts were then used to calculate the relative composition by first using the species cross-section to convert the recorded counts to true scattering counts using the following relation:

$$C_t = \frac{C_{obs}}{S_i} \approx \frac{C_{obs}}{R(\frac{d\sigma}{d\Omega})} \tag{4}$$

Where C_t is the true count, C_{obs} is the observed counts, S_i is the yield factor, R is a constant relating to the experimental parameters, and $\frac{d\sigma}{d\Omega}$ is the cross section [44].

It was then assumed that the final sputtering composition matched that of the bulk [56]. The known bulk composition ratio 42Ag:42In:16Yb was therefore used to derive the true composition for each spectrum by count ratio comparison. The composition change through both sputtering cycles was then plotted and can be found within the results section. Further discussion of the Gaussian parameters and fitting methods used for each spectrum can be found in Appendix C.

3.4 Vesta and STM Simulation Methods

3.4.1 Vesta Modelling

Vesta software [45] was used to analyse the theoretical bulk and make comparisons to the motifs seen in STM images. Vesta allowed easy manipulation and isolation of various elements of the structure. Primarily, Vesta was used to identify cluster centre planes. These planes were then isolated and projected such that we were able to see their geometry along the (111) direction.

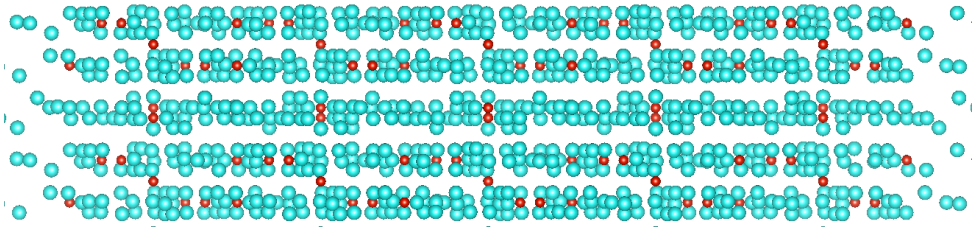


Figure 5: Vesta structural model showing Yb (turquoise) and cluster centres (red). In the figure, the page portrait direction is the (111) direction. Clear plane progressions can be seen between Yb subplanes.

The measure tool in Vesta was then used to identify the exact atom coordinates, which in turn allowed measurement of coplanar distances using basis conversion and basic vector calculations. We performed motif measurements for all 10 identified Yb-rich subplanes. We also imported images of these Vesta planes into Inkscape. This allowed transposition of rough shapes onto the images to map the motifs present.

These reduced maps were then, in turn, transposed onto the STM images and analysed along with our known Vesta and STM motif sizes to check for possible matches. All clear STM images were sampled in order to minimise fit uncertainty, with this procedure allowing rough identification of all present motifs.

3.4.2 Computational Comparisons

Our final method for plane identification involved the use of a computational STM model. This model was constructed using the Tersoff-Hamann model of tip contribution [46]. This allowed us to model contributions to the LDOS from each species as 2-dimensional Gaussians. The physics and implementation of this model are discussed within Appendix D.

The imported atomic coordinates of the bulk were used to model our plane contributions. Our model had 4 primary inputs: a plane thickness (dz), plane centre location (z), plane number (n), and finally a direction (± 1) encoding whether we were looking up through the plane or down. Using this and our known Vesta coordinates in the (111) basis, we were able to generate simulated STM images of specific planes, varying the plane thickness, the number of plane contributions included and the surface orientation. We then matched these STM model images to our real images by visual inspection, followed by comparison of motif sizes from Vesta calculations.

Throughout the modelling process, we included both Yb and non-Yb-dominated planes. We did this to verify that our motifs couldn't have arisen from non-Yb-rich planes. Additionally, for all planes, the minimum dz value used was set to be dz=0.5 Å. This choice was made to match the minimum density of planes analysed with that of the pure elemental crystal. For instance, the FCC structure of pure Ag has a spatial Ag density of 0.06 atoms per $\mathring{A}^3$ [47]. This minimum thickness requirement was implemented to ensure we only surveyed structurally stable planes [48]. All thicker dz gave higher densities or matched the minimum viable density. The matching process was completed for all 10 subplanes over a dz range of 0.5 Å-3 Å ie 1-6 plane contributions included. The plane start point (z) was also varied to check for differences which may arise from relaxation or cleavage.

4 Results and Analysis

Here we present the findings of all experiments alongside our analysis and interpretation of these results. In this section specifically, we will construct a surface termination model and present it with support from our various experimental data sources.

4.1 STM Analysis

4.1.1 Observed Stepheights

Over the 9 large-scale images, 121 step-height measurements were made. These were then plotted in histogram format, giving rough Poisson profiles. Then, using the histogram bin centres as x coordinates and the frequency density as y coordinates, χ^2 analysis was used to fit Gaussian profiles to the step-height distribution. Analysis of the reduced χ^2 for several fits produced a most likely fit that demonstrated 4 distinct step height Gaussians with means of: 3.7±0.3 Å, 4.4±0.2 Å, 5.6±0.3 Å, and 1.1±0.4 Å.

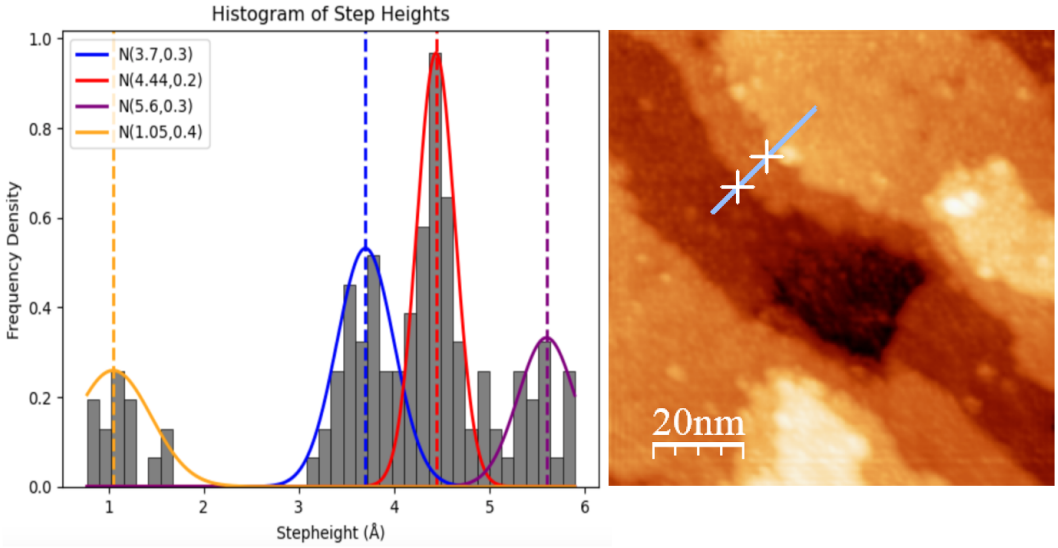


Figure 6: Left hand image: Histogram showing measured step heats with Gaussian fit overlayed. Legend format: (Mean, Standard deviation). We can see 4 clear Poisson curves with high sample-size related noise, Right Hand image: Large scale STM image from our dataset showing clear terrace transitions one is labelled using a line profile.

The relatively poor uncertainty in these step heights can be attributed to the limited sample size available. This was also reflected in the relatively poor reduced χ^2 of 5.4 for our best-fit Gaussian model. Addressing this with further STM experiments may be necessary to lower these height uncertainties. However, the range of error and reduced χ^2 is likely more consistent with random sample noise and resolution limitations rather than fundamental model fitting errors. Consequently, it is probable that the 4-step step-height model falls within acceptable uncertainty

limits.

4.1.2 Theoretical Bulk Stepheights

Using our Vesta bulk model, we were able to identify a possible explanation for our step height measurements. As we have already alluded to, the structure is segregated into 3 successive Yb-rich planes containing cluster centres. We may further subdivide these principal planes into individual Yb planes or subplanes, with C containing 4 distinct Yb layers, and A and B containing three. These sublayers are roughly separated by 1 Å steps, with an example visualised in the figure below:

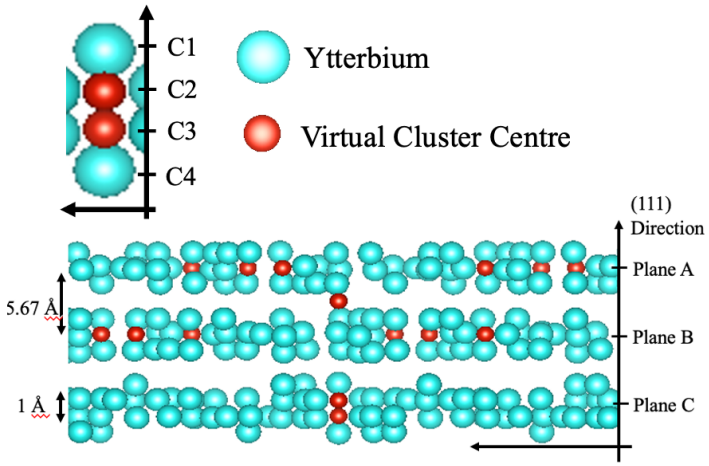


Figure 7: Vesta image showing section of bulk structure oriented along (111) direction to show plane progression. Top image is a magnified C plane highlighting C subplane progressions.

We expect that the progression of these planes should follow that seen in the Vesta visualisation, proceeding from A to B to C. If it were the case that we saw only top-of-plane to top-of-plane transitions, we would observe a uniform step-height of 5.67 Å. However, from our collected step-height data, this model appears inaccurate. Instead, we allow our surface to terminate at any subplane level, giving a range of possible step-heights of: 1 Å, 3.5 Å, 4,5 Å, and 5.7 Å. These correspond to various transitions. For instance, A2 to B1 or B2 to C1. These subplane transitions appear to fall within the range of uncertainty of our measured step-heights. Hence, we suggest that our surface terminates along these subplanes.

4.1.3 STM motifs

Using the small-scale STM images, local motifs were able to be identified. The identified motifs were measured for size and internal angles using the method described in Appendix B. From these measurements, 4 distinct surface motifs were identified, including: regular equilateral triangles (A), irregular-tight triangles (B), uniformly coloured equilateral triangles (C), and diffuse spirals (D).

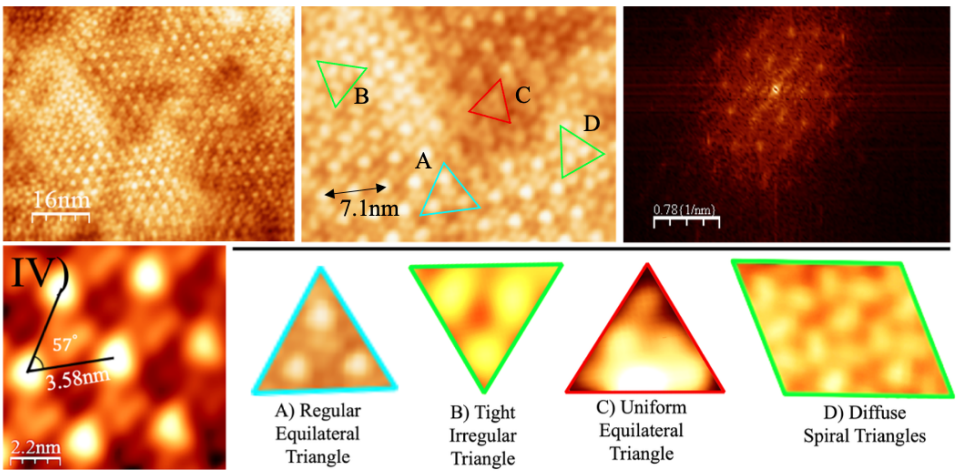


Figure 8: I) Large scale image showing STM surface after cleaning along with clear motifs. II) Magnified section of I) showing motifs with greater resolution. Several common motifs can be seen with the image mostly being spanned by regular triangular arrays of atoms. III) Fourier transform of the STM image showing hexagonal motif symmetry. IV) High resolution image of regular triangle motif (A) with atomic distance and internal angle labelled. A-D) Identified surface motifs with names labelled.

Motif	Side Length (nm)	Internal Angle (°)
Regular Triangle (A)	3.58 ± 0.03	57 ± 1
Tight Triangle (B)	1.85 ± 0.03	49 ± 1
Uniform Triangle (C)	3.73 ± 0.06	59 ± 1
Spiral (D)	2.21 ± 0.04	N/A

Table 1: mean motif sizes and angles

Importantly, unlike previous approximant studies [49], no periodic relationship could be identified between motifs. For instance, large triangles mostly formed in arrays of inconsistent size and location across the STM image, with similar distributions being observed for all motifs. Finally, in accordance with the 1/1 approximant model, we expected to see clear motif orientation transitions between planes, which were not observed [50]. The principal example being that the theoretical A and B planes are mirror images of each other along the x=y plane. Thus, motifs in A and B planes should be rotated 180^o relative to each other. This transition was also not observed.

4.1.4 Theoretical Surface motifs

Using the subplane model, individual subplanes were isolated in Vesta. This allowed us to visualise the species present at the plane surface as well as the influence of subsequent/substrate planes. For each of these planes, the motifs were measured for possible matches to our 4 motif

patterns. From these Vesta models, we identified the C1, C2 and C3 planes as being possible candidates to explain the motifs observed. For example, C1, being visually less Yb dense, demonstrated large triangular Yb structures of side length 4.1nm, similar to that of the uniform triangular motifs (Figure 9). All additional motifs could be explained using C2 or C3 planes, as partially demonstrated in the figure below.

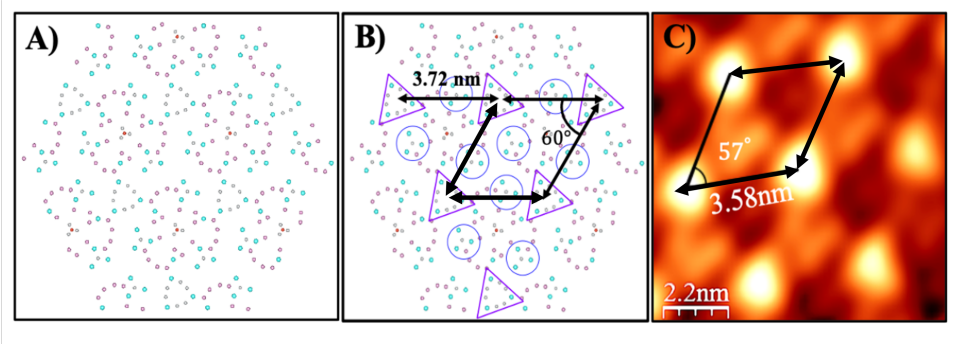


Figure 9: A) Unaltered Vesta image of plane C1 with (111) direction pointing into page. B) Overlay of rough motif shapes and sizes onto same C1 plane. C) Example of similar motif to observed Vesta model matching shape, size and orientation. A rhombus is overlayed to allow better image comparison.

From this, we concluded that the surface demonstrated large amounts of subplane transitions. Different subplanes have distinct motifs, thereby explaining the inconsistent motif distribution. We believe that these subplanes planes are likely similar in surface free energy and are only separated by small step heights. This means they may be able to easily interchange across the surface, creating the incoherent motif arrangements observed. These transitions are additionally supported by height analysis studies of the images, showing different motifs appearing at different relative height levels, indicating they belong to different subplanes. The data and plots for this height analysis can be seen in Appendix A.

Given observed A and B step heights, similar visualisations were made of the A and B planes, which are shown in Appendix D. These demonstrated remarkably similar motifs to C subplanes. However, the problem of missing motif mirroring still remained, as all A and B Vesta motifs observed were inverted mirror images.

4.1.5 Computational STM motifs

Given that STM only shows contribution to the LDOS for a specific bias-dependent energy range, our Vesta models could not be used to fully visualise motifs. For example, In or Ag dense motifs like the ones below in figure (10) would appear significantly weaker under positive bias. This occurs due to the lack of filled states near the Fermi level compared to Yb, limiting their contribution to the tunnelling current [51]. Therefore, to compensate for this, each of

our Vesta planes were fed into our computational STM model to visualise these effects as well as the effects of convolution with lower layers. Note: In visualising the effects of various depth effects, the range of z coordinates was varied to include and exclude certain atomic contributions and compare subplane transitions. This variation process produced simulations similar to the following:

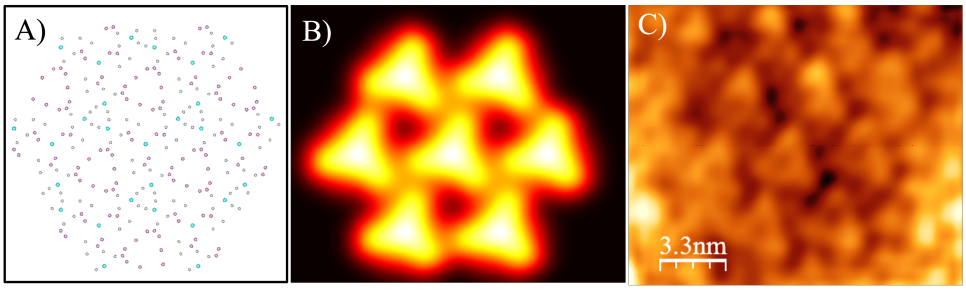


Figure 10: A) Vesta image of C2 plane showing regular arrays of Yb (turquoise) and In (Pink) triangles. B) Computational modelling of same Vesta planes showing uniform brightness equilateral triangles. C) Comparison STM image with matching array of regular triangles of similar size.

From these simulations, we were able to confirm the similarity of C plane motifs to those observed. Additionally, we were able to observe that A and B STM simulations produced superficially similar motifs with no motif inversions despite their inverted structures.

We believe this arises due to STM convolution effects. STM only gives us an image of the LDOS at the surface, although the contribution does decay with distance from the tip, neighbouring layers of atoms just below the top layer do contribute to the LDOS and therefore the motifs seen under STM analysis. We believe that because A and B are inverted, we see different lower layers contributing to the LDOS and therefore different motifs. For example, A1 is the equivalent of B3. Therefore, as we look down at A1, we see contributions from A2 and A3. Meanwhile, as we look down through B1, we see contributions from B2 and B3, i.e., A2 and A1. So fundamentally, even though A and B motifs should be mirror images, the differing lower layers completely distort this relationship. So, when we look at A and B subplanes, we are observing a completely different LDOS. The overall distortion effects from looking through these planes produce motifs that appear superficially similar but appear in reverse order to their A/B counterpart. For instance, in A, the regular triangles were the middle motif corresponding to A2; however, in B, it corresponds to the top B1 layer. Height analysis of our confirmed A/B transition with atomic resolution was able to confirm this shift in motif transition ordering (see Appendix A), which, along with our matching STM simulations, provides credible evidence that this convolution effect may be present. Direct DFT studies of the surface should be able to confirm this hypothesis within further studies.

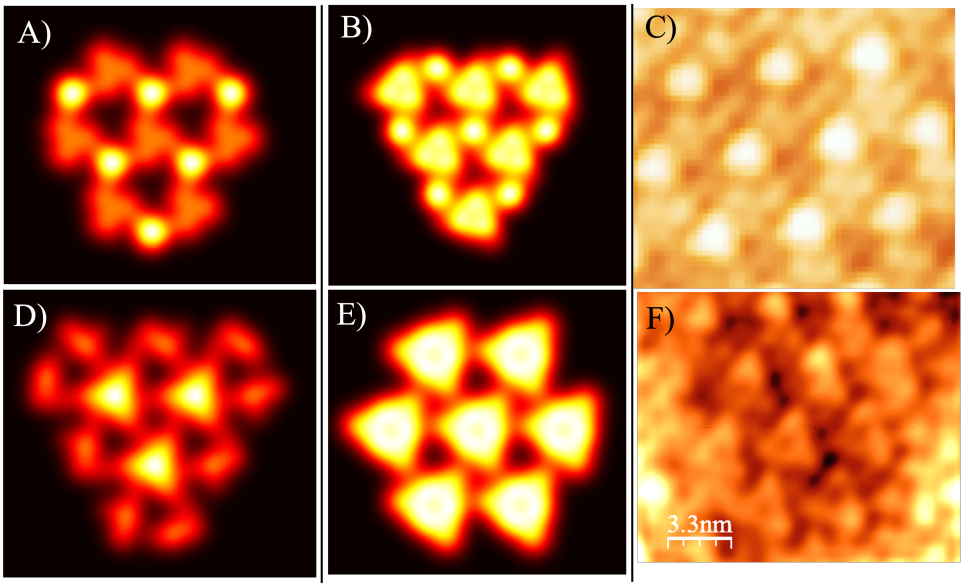


Figure 11: Overall this figure compares A and B motifs to show similarity under STM simulation. A) A1 subplane simulation showing regular triangle Motifs. B) B2 plane simulation showing similarly orientated triangle motifs. C) Comparison STM example showing internal triangles as too low resolution to distinguish A and B planes. D-F) Same structure as A-C) for different motif. ie D shows A2 simulation and E shows B3 simulation. F) shows matching orientation for macro scale motifs

It is important to note that the simulation model used is limited in reliability, given its lack of modelling of tip geometry, tip shell contribution or hybridisation of shells on the sample surface. The effects of this uncertainty were combatted by only using Vesta bulk measurements to estimate theoretical motif sizes. This prevented confirmation bias or false motif visualisations from affecting our model fits. The convolution explanation of A and B orientation is, however, dependent on our simulation model. Hence, although it is partially supported by other evidence, it should be considered with care until DFT studies can confirm its validity.

4.2 LEIS Analysis

Using our spectra data, a plot of relative composition vs sputtering dose was constructed for the two sputtering rounds. The composition charts below both appear to be In and Yb enriched with the relative peak (post annealing) compositions given in Table 2. It was additionally noted that the surface composition appeared to be Ag-depleted.

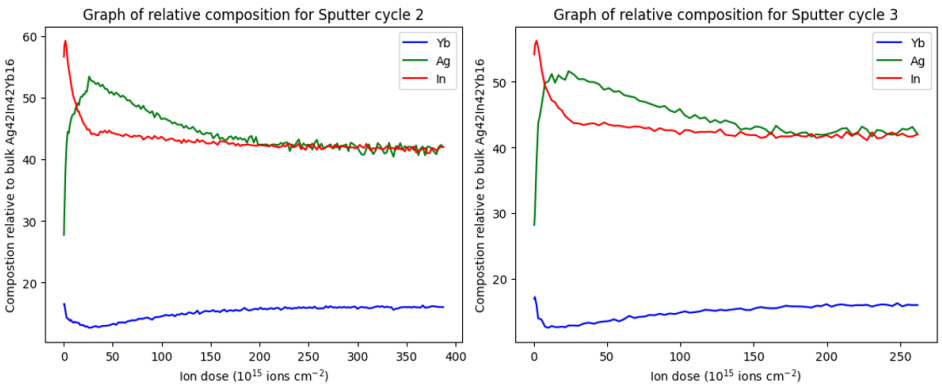


Figure 12: Left-hand plot shows composition vs dose for sputter cycle 2. We can see an initial In richness and Ag depletion which rapidly stabilises as we reach the bulk. Right-hand plot shows sputter cycle 3 and demonstrates a similar trend. The peak compositions correspond to the post-annealing (ie surface) composition with the first few sputtering doses removing accumulated oxides from the 2 hour post annealing cooling period.

Species	Sputter 2: Atomic Composition	Sputter 3: Atomic Composition	Bulk Composition
Indium	59.28 ± 0.02	56.21 ± 0.03	42
Ytterbium	15.41 ± 0.04	15.99 ± 0.02	16
Silver	38.07 ± 0.03	37.74 ± 0.03	42

Table 2: Table showing composition peaks for each sputter cycle along side bulk composition.

4.2.1 Composition Matching

We were able to use the peak compositions to search for matching theoretical planes. This search was conducted by splitting the sample into multiple 0.5 Å slabs in Python and then taking the weighted ratio of Yb, In, and Ag atoms detected within that slice. Using this slab method, six plane candidates were identified corresponding to the C2, C3, A2, A3, B1, and B2 subplanes. All of these plane terminations were close to or contained an In-rich and Ag-depleted plane. Furthermore, all had similar compositions to the peak compositions given in Table 2.

Species	Predicted Composition	C1/C4 Composition	A1/B3 Composition	B2/A2 Composition
Indium	59.28 ± 0.02	55.56	57.58	55.10
Ytterbium	15.41 ± 0.04	16.05	15.15	16.33
Silver	38.07 ± 0.03	28.40	27.27	28.57

Table 3: Table showing best match to indium rich surface planes. Due to space the remaining matches are listed within Appendix C.

This tentatively matched our STM subplane model, with the predicted composition of the

subplanes being within the range of uncertainty of our LEIS composition data.

Additionally, the slight discrepancies between our predicted compositions and our measured compositions may also be explained by fundamental uncertainties within our LEIS methodology. Principally, the assumption that the LEIS cross sections for Ag, In, and Yb detection were the same as in the previously tested Quasicrystal samples, and that the fully sputtered composition matched that of the bulk. Both of these assumptions introduce small uncertainties. For example, the theoretical bulk may not match the real structure due to possible density discrepancies or differences in the holistic chemical environment on the surface. Both of which would considerably affect the cross-section for each species, as well as, the final post-sputtering composition. These fundamental uncertainties are unfortunately inherent to any LEIS analysis and can only be constrained by its use in conjunction with other methods such as STM. Given the profile match between our STM model and the LEIS data, we are confident that the effects of these uncertainties were minor. However, further analysis of cross sections and the natural bulk would still be beneficial to constrain this uncertainty.

We also have to consider one additional explanation for the observed In richness beyond our model. That being that In atoms, as the most chemically stable of the species present in the approximant, may be able to translocate during the annealing process. This may form a pure elemental indium layer near the surface of the sample. The layer would present as high In abundance, and Ag depletion with the layer shadowing Ag signals. This phenomenon has been confirmed before in intermetallics containing In metal and thus, cannot be discounted as an explanation of the high In surface abundance [52]. XPS analysis of the surface may be needed to fully discount this hypothesis and constrain our plane model by detailing the surface composition within the first few nm of the sample.

5 Discussion of Surface Stabilities

5.1 Model Overview

From our experimental analysis above, we now know that the structure terminates along 3 principal major planes. These termination planes are rich in Yb atoms. We also propose that the STM images then demonstrate further subdivision of these major planes into Yb subplanes with small terrace steps observed between subplanes. Furthermore, from our LEIS analysis and STM modelling, we can surmise that the major subplanes present are C1, C2, C3, and C4; meanwhile, only A2, A3, B1, and B2 are present, with the C2-A1-B3 subplane progression being the most abundant based on our step-height commonalities.

5.2 Chemical Stability Analysis

Having concluded that the experimental evidence may suggest the existence of subplane terminations as well as large-scale step heights between adjacent cluster centre planes. We must now ask why these plane terminations are more favourable than others. Within this section, we will present an analysis of the chemical favourability of these planes, demonstrating energetic profiles in concordance with our experimental model hypothesis.

5.2.1 Areal Density Studies

Within surface formation theory, when terraces form, bonds between the plane and the cleaved plane above are broken, leaving dangling bonds [53]. The greater the density of a certain bonded species within a single plane, the greater the ratio of coplanar bonds to dangling bonds. Consequently, high-density planes are often more chemically stable than lower-density planes due to the shorter bond lengths and fewer dangling bonds. Within the Tsai cluster model of our approximant, we know Yb atoms are only bonded to other Yb atoms. Considering the large size of Yb atoms, long or cross-plane bonds are very likely to be weak. Hence, planes with low Yb density will have more long Yb-Yb bonds and more Yb dangling bonds. This renders the plane highly unstable relative to higher-density Yb planes [54].

Using a slab model, we were able to iterate through the bulk and derive areal densities for Yb atoms. The area cross-section of the plane was derived using a simple cross-product analysis with the sample being split into uniformly sized parallelogram planes. This produced the following plot of Yb density vs position along the (111) vector direction:

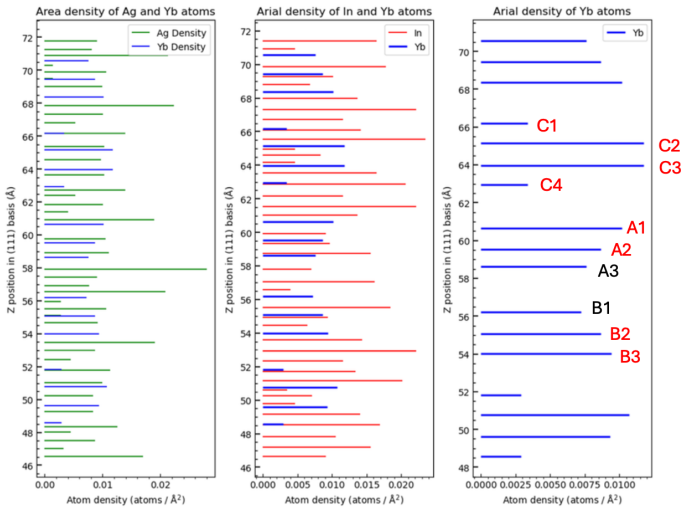


Figure 13: Three fold comparison figure showing the arial density of species throughout the strucuture. The Z coordinate start values are arbitrary with data being taken from a 80 Å section (ie showing all 4 subplanes). The first graph is a comparison of Ag and Yb, the second (middle) is of In and Yb and the right hand plot is Yb. We have included the third plot to allow the reader to identify the subplanes clearly, the group of 4 peaks is plane C from which others can be derived. Note the x scale on the Yb only plot is adjusted for clarity and is not the same as used in the other plots.

As can be seen in the above figure, C2 and C3 subplanes appear to be the most dense, supporting the experimental model in which they both appear as surface termination planes. B3 and A1 are also similarly Yb-rich, however, to a lesser extent than C2 and C3. Moreover, B2 and A2, both observed plane terminations, are of relatively low Yb density. The question of why the low-density C1, C4, A2 and B2 planes are observed still remains unanswered using Yb density alone. Instead, in line with the LEIS evidence of relative In abundance and Ag paucity, the same density studies were repeated for Ag and In.

From the density profiles, we can clearly see that C1, C4, A2 and B2 form alongside very high density In planes. We believe that, similar to the role of Al in Au-Al-Tb quasicrystal, the lower surface free energy indium is able to chemically support the relaxing Yb layer above [55]. This electronic support stabilises the plane energetically. This increases the likelihood that the surface terminates at these planes during the annealing process. Consequently, this may explain the observed presence of these planes within the STM data. The confirmation of this stabilisation effect should be possible using DFT to derive the local density of states contributions from the stabilising In layer.

5.2.2 Cluster Centre Analysis

Previous studies on Au-Al-Tb [55] and 1/1 Ag-In-Yb approximant [56] have shown that these high Yb density planes form invariably at the location of Tsai cluster centre planes. Previous work has also demonstrated a clear link between rare earth density and plane stability [57]. We have previously surveyed the cluster centre plane locations, identifying that C2, C3, A2, and A3 are all cluster centre planes in line with this theory. However, we have not analysed the number of cluster centres split by each plane as a possible explanation for plane stability.

Tsai clusters represent the most energetically favourable arrangement of atoms within the bulk structure. Consequently, planes which intercept and cleave a larger number of these clusters destabilise the surrounding structure, making their formation energetically unfavourable [57]. This was identified within the Au-Al-Tb structure by the apparent absence of intermediary planes in the unit cell, which cleaved a larger number of cluster centres [55]. With this approximant being similar to the 1/1 In-Ag-Yb approximant, we suspect a similar chemical trend may appear in our structure. Hence, the In and Yb-rich planes may correspond to those which cleave

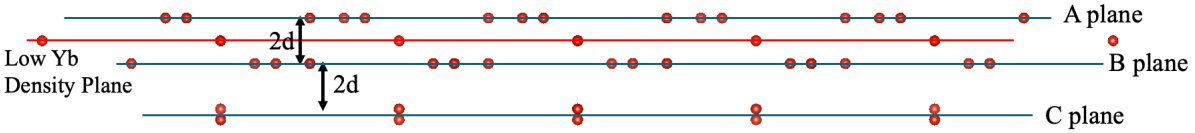


Figure 14: Labelled diagram showing cluster centres (red circles). The planes are labelled for clarity with 2d being the total cluster height hence we see A and B are separated by one cluster width. The low density plane between A and B is also shown to allow cluster cleavage counts to be made.

In determining the veracity of this model, we projected our structure along the (111) axis and counted the number of clusters cleaved for each subplane type. From the diagram (Figure 14), we can see that both C2 and C3 only cleave 2 clusters per 3 preserved. This occurs due to C2 being collinear with the bottom of the clusters contained in the B2 subplane and C3 being collinear with the top of the A2 clusters. This also means that the A2 and B2 cluster planes also cleave 3 clusters per 2 preserved.

Qualitatively, this may indicate that there is no cluster-driven preference behind the appearance of any of the principal planes. This means A is as likely to form as B or C. It does equally indicate that non-cluster-centre subplane layers, such as C1, cleave large numbers of cluster centres, approximately 5 per unit cell. (The same number of 5 cleaved per unit cell was calculated for B1, B3, A1, and A3 as well.) Consequently, it is possible that these planes are less energetically stable and are present due to the stabilising effects of the nearby In-rich planes. We can also note that the Yb-poor cluster-centre plane between A and B also likely doesn't appear in the

plane progression due to its low density relative to its high number of clusters cleaved (4 per 1 preserved).

With cluster centre planes being highly stable in other similar quasicrystals, we would expect the structure to show preferential cleaving along the principal cluster centre containing planes. For example, C2 and C3 should form longer terraces than C1 or C4. Further STM analysis showing plane divides would be necessary to confirm such relative stability conclusions, with less stable planes often being shorter and appearing less often. Unfortunately, our data was too low resolution within large-scale images to differentiate plane types and make area measurements. Furthermore, the sample size of the images was too small compared to the high similarity of motifs to make accurate commonality measurements.

5.2.3 Glue Atoms

One additional chemical influence on the stability of planes is the presence of non-cluster-based Yb glue atoms. These atoms bond Tsai clusters together, stabilising the bulk structure. These glue atoms, given their higher bond lengths and lack of stabilisation from multiple cluster bonds, have been linked to lower surface stability when found in high abundance within planes [57].

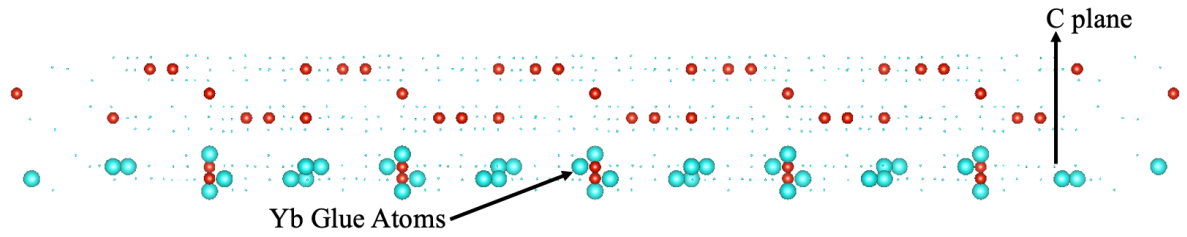


Figure 15: Labelled diagram showing glue atoms (large turquoise circles), cluster centres (red circles), and Yb cluster atoms (small turquoise dots). A c plane is labelled showing it to be the only plane with glue atoms with the highest density located within the middle 2 subplanes (ie C2 and C3).

In our bulk model, the only plane to contain such glue atoms was plane C, containing 10 Yb glue atoms per unit cell. Furthermore, we identified C2 and C3 as having the highest number of Yb glue atoms relative to Yb cluster atoms. This may provide another possible explanation for why we observe C1 and C4 despite their higher number of cleaved clusters and lower Yb density. Additionally, with both having higher density In planes nearby and lower glue atom ratios, this may render them similarly stable to C2 and C3 planes, possibly refuting the predicted difference in their abundances within the previous section.

5.2.4 Screw Defects

On a final note, one of the principal pieces of evidence we have for the relative energetic similarities between all planes is the high frequency of screw defects observed. In the 1/1 Ag-In-Yb approximant, the presence of screw defects was linked to energetic similarity between planes. This allowed easy migration of species between planes during the annealing process. This led to the formation of these screw defects as a byproduct of this large-scale migration [51].

Of the 4 small scale images showing two distinct planes, 3 of them showed screw defects. We believe all of these appeared to be transitions between A and B planes. Combined with the fact that both are mirrors of each other, these defects render the possibility of them being approximately energetically degenerate quite plausible. Hence, it is possible that A and B planes should appear with the same abundance, with neither being more energetically favourable.

6 Conclusions and Further Work

We have successfully analysed the (111) surface of the 2/1 approximant using both STM and LEIS analysis. From these methods, we have identified that the approximant likely terminates along 3 principal planes A, B and C, which are both Yb-rich and collinear with the location of cluster centre planes. This is similar to previously observed quasicrystal plane termination trends. Using STM analysis, the surface was also identified as possibly forming subplane divisions between the various Yb-rich layers within these larger planes. We believe these subplanes are able to form due to a mixture of chemical effects. For example, limiting the cleavage of stable Tsai clusters. We also believe that the planes show no preferential formation due to a fine balance between these varying chemical effects. This is demonstrated through frequent transitions between subplanes, producing a complex stochastic surface profile. Further work on this unique termination structure may provide novel catalysis applications and may encourage further investigation into the difference between coarse approximants and their parent quasicrystals.

That being said, due to our small sample size, further work will be needed to fully confirm the validity of these formation trends. We highly recommend that the following extra work be completed to address the issues highlighted:

- XPS work to confirm the In stability hypothesis by checking for a migrated In elemental layer.
- Further STM work imaging terrace transitions to provide commonality data and give a reference for plane stability.
- Improvements to computational modelling work or use of DFT to confirm the A-B plane convolution hypothesis.

Bibliography

[1] Author not publicised, Dan Schechtman - The Prize's legacy, National Institute of Science and Technology, Aug 2021, Accessed: Mar 2026, https://www.nist.gov/nist-and-nobel/dan-shechtman/person-behind-nobel-prize-dan-shechtman

[2] W.Steurer, Twenty years of research on quasicrystals Part I, Zeitschrift für Kristallographi, Vol 219, 2009, DOI: https://doi.org/10.1524/zkri.219.7.391.35643

[3] A.I Goldman, R.F Kelton, Quasicrystals and Crystalline Approximants, American Physical Society, Reveiws of Modern Physics, Vol 65, 1993, https://doi.org/10.1103/RevModPhys.65.213

[4] P.Kramer, R.Neri, On periodic and non-periodic space fillings of Em obtained by projection, Acta Cryst, Vol 40, 1984, DOI: https://doi.org/10.1107/S0108767384001203

[5] N.G Bruijn, Algebraic theory of Penrose's non-periodic tilings of the plane, Indagationes Mathematicae, Volume 84, 1981, DOI:https://doi.org/10.1016/1385-7258(81)90016-0

[6] S.Coates, Metallic mean fractal systems and their tilings, Journal of fractal geometry, Volume 1, 2025, DOI: 10.4171/JFG/170

[7] M.Baake, A Guide to Mathematical Quasicrystals. J.Suck, M.Schreiber, P.Häussler, Springer Series in Materials Science, vol 55, 2002, Springer, Berlin, Heidelberg. https://doi.org/10.1007/978-3-662-05028-62

[8] M.Schreiber, J.Suck, P.Haussler, Quasicrystals: An introduction to Structure, Physical Properties and Applications, Springer, 2002, ISBN: 3-540-64224-2

[9] S.Coates, Quasicrystals as catalysts for the steam reformation of methonal, Mphys Project University of Liverpool, 2015

[10] C.Duang, The concept of the approximants of quasicrystals, Scripta Metallurgica et Materialia, Vol 33, 1995, https://doi.org/10.1016/0956-716X(95)00149-P

[11] C.Cui , P.J.Nugent, M.Shimoda, J.Ledieu, V.Fournée, A.P.Tsai, R.McGrath, H.R.Sharma, The atomic structure of the threefold surface of the icosahedral Ag-In-Yb quasicrystal, J Phys Condensed Matter, 2012, DOI: 10.1088/0953-8984/24/44/445011

[12] Introduction to Solid State Physics, C.Kittel, 8th edition, Wiley, 2005, ISBN: 0-471-41526-X

[13] M.ladd, R.Palmer, Structure Determination by X-ray Crystallography, Chapter 2, 2nd edition, 1983, Springer, ISBN: 978-1-4614-3956-1 (5th edition ISBN)

[14] H.R.Sharma, Lectures on Surface Science: Lecture 4, University of Liverpool

[15] K.Oura, M.Katayama, A.V.Zotov, V.G.Lifshits, A.A. Saranin, Surface Science: An Introduction, Chapter 5, Springer, 2003, ISBN: 978-3-642-05606-2

[16] H.R.Sharma, Lectures on Surface Science: Lecture 4, University of Liverpool

[17] K.Oura, M.Katayama, A.V.Zotov, V.G.Lifshits, A.A. Saranin, Surface Science: An Introduction, Chapter 10, Springer, 2003, ISBN: 978-3-642-05606-2

[18] J.Shackleford, Introduction to Materials Science for Engineers, Upper Saddle River, 2009, ISBN: 978-0-13-601260-3

[19] J. Bamberg, G. Cairns, D. Kilminster, The crystallographic restriction, permutations, and Goldbach's conjecture, American Mathematical Monthly, 2003, DOI:110(3):202–209

[20] R.Penrose, Pentaplexity a class of Non-periodic tilings of the plane, Mathematical Intelligencer, Volume 2, 1979, DOI:10.1007/BF03024384

[21] M.Schreiber, J.Suck, P.Haussler, Quasicrystals: An introduction to Structure, Physical Properties and Applications, Springer, 2002, ISBN: 3-540-64224-2

[22] A.Haynes, Introduction to mathematical quasicrystals, Online Lecture notes, https://www.math.uh.edu/ha accessed 14/11/25

[23] H. Sanger, Surface Structure and Epitaxy on Ag-In-Rare Earth Quasicrystals and Related Approximants,, Phd Thesis, University of Liverpool, 2015

[24] C.Cui, H.R.Sharma, STM Study on the (100) Surface of the AgInYb 1/1 Cubic Approximant, Acta Physica Polonica, Volume 126, DOI:10.12693

[25] H.Takakura, C.P.Gómez, A.Yamamoto, M.Boissieu, A.P.Tsai, Atomic structure of the binary icosahedral Yb–Cd quasicrystal, Nature Materials, Vol 6, 2007, DOI: https://doi.org/10.1038/nmat1799

[26] S.Smaalen,J.DeBoer, Y.Shen, Six-dimensional structure model for the icosahedral quasicrystal, Physical Review B, Volume 43, 1991, DOI:10.1103/PhysRevB.43.929

[27] C.Cui , P.J.Nugent, M.Shimoda, J.Ledieu, V.Fournée, A.P.Tsai, R.McGrath, H.R.Sharma, The atomic structure of the threefold surface of the icosahedral Ag-In-Yb quasicrystal, J Phys Condensed Matter, 2012, DOI: 10.1088/0953-8984/24/44/445011

[28] S.Coates, K.Nozawa, M.Fukami, K.Inagaki, M.Shimoda R.McGrath, H.R.Sharma, R.Tamura, Atomic structure of the (111) surface of the antiferromagnetic 1/1 Au-Al-Tb approximant, Physical Review B, Vol 102, 2020, DOI: https://doi.org/10.1103/PhysRevB.102.235419

[29] H.R.Sharma, Lecture notes on Surface Science, Lecture 6

[30] W.Umranth, Fundamentals of Vacuum Technology, Pg 68-70, Commercial Article: Oerlikon Leybold Vacuum, 1990, https://mmrc.caltech.edu/Vacuum/Leybold/fvt_fundamentals_of_vacuum_technology_e

[31] J.W.Rabalais, Principles and Applications of Ion Scattering Spectrometry: Surface Chemical and Structural Analysis, Wiley, 2003, ISBN: 0-471-20277-0

[32] S.Lounis, Theory of Scanning Tunneling Microscopy, Lecture published to ArXiV, 2014, DOI: https://doi.org/10.48550/arXiv.1404.0961

[33] C.J.Chen, Introduction to Scanning Tunneling Microscopy, Chapter 2, 2nd Edition, Oxford University Press, 2007, ISBN: 9780199211500

[34] H.R.Sharma, Lecture notes on Surface Science, Lecture 7

[35] C.Chen, Role of Tip Material in Scanning Tunneling Microscopy, Springer Nature, Vol 159, 2011, DOI: https://doi.org/10.1557/PROC-159-289

[36] G.Mandi, K.Palotas, Chen's derivative rule revisited: Role of tip-orbital interference in STM, Phys Rev B, Vol 91, 2015, DOI: https://doi.org/10.1103/PhysRevB.91.165406

[37] H.R.Sharma, M.Shimoda, A.P.Tsai, Quasicrystal surfaces: structure and growth of atomic overlayers, Advances in Physics, Vol 56, 2007, DOI: https://doi.org/10.1080/00018730701269773

[38] B.Bolliger, M.Erbudak, A.Hensch, D.D.Vvedensky, Surface structural phase transitions on icosahedral Al–Pd–Mn, Materials Science and Engineering A, Vol 294, 2000, DOI: https://doi.org/10.1016/S092

5093(00)01078-9

[39] I. Horcas, R.Fernandex, J.M.Gomez-Rodriguez, A software for scanning probe microscopy and a tool for nanotechnology, review of scientific instruments, volume 78, 2007, DOI: 10.1063/1.2432410

[40] H.H.Brongersmaa, M.Draxlerc, M.de Riddera, P.Bauerc, Surface composition analysis by low-energy ion scattering, Surface Science Reports, Vol 62, 2007, DOI: 10.1016/j.surfrep.2006.12.002

[41] C.V.Cushman, P.Bruner, J.Zakel, G.H.Major, B.M.Lunt, N.J.Smith, T.Grehl, M.R.Linford, Low energy ion scattering (LEIS). A practical introduction to its theory, instrumentation, and applications, Analytical Methods, vol 8, 2016, DOI: 10.1039/c6ay00765a

[42] T.Hosokawa, K.Yamada, Ion neutralization factor measurement for low energy electron beams, NIMA Section A, Vol 420, 1999, DOI: https://doi.org/10.1016/S0168-9002(98)00895-X

[43] D.A.Bromley, Treatise on Heavy-Ion Science, Chapter 3, Springer Nature, 1985, Accesed online (12/03/26), e-ISBN: 978-1-4615-8103-1

[44] H.H.Brongersmaa, M.Draxlerc, M.de Riddera, P.Bauerc, Surface composition analysis by low-energy ion scattering, Surface Science Reports, Vol 62, 2007, DOI: 10.1016/j.surfrep.2006.12.002 (cited [40] also)

[45] K.Momma, F.Izumi, VESTA.3 for three-dimensional visualization of crystal, volumetric and morphology data, Journal of Applied Crystallography, 2011, DOI:10.1107/S0021889811038970

[46] R.Gaspari,* S.Blankenburg, C.A.Pignedoli, P.Ruffieux, M.Treier, R.Fasel, D.Passerone, s-orbital continuum model accounting for the tip shape in simulated scanning tunneling microscope images, Physical Review B, Vol 84, DOI: 10.1103/PhysRevB.84.125417

[47] J.W.Arblaster, Selected Values of the Crystallographic Properties of the Elements, ASM International, 2018, Acessed online: 12/03/26, E-ISBN: 978-1-62708-155-9

[48] Z.Padopalis, G.Kasner, Thick atomic layers of maximum density as bulk terminations of quasicrystals, Physical Review B, Vol 72, 2005, DOI: https://doi.org/10.1103/PhysRevB.72.094206

[49] S.Coates, D.Burnie, H.R.Sharma, R.McGrath, Scanning Tunnelling Microscopy Studies of Tsai-Type Quasicrystal Approximants, Israel Journal of Chemistry, vol 64, 2024, DOI: https://doi.org/10.1002/i

[50] C.Cui, H.R.Sharma, STM Study on the (100) Surface of the AgInYb 1/1 Cubic Approximant, Acta Physica Polonica, Volume 126, DOI:10.12693

[51] C.Cui, H.R.Sharma, STM Study on the (100) Surface of the AgInYb 1/1 Cubic Approximant, Acta Physica Polonica, Volume 126, DOI:10.12693 (cited previously 3 times)

[52] A.Y.Alfahad, V.K.Singh, E.Gaudry, J.Ledieu, V.Fournée, P.Gille, A.M.Gardner, P.R.Chalker, R.McGrath, H.R.Sharma, Atomic Structure, Chemical Composition, and Oxidation Behavior of the (001) Surface of Ni2In3 Intermetallic Catalyst, Physical Review Materials, Vol 9, 2025, DOI: https://doi.org/10.1103/PhysRevMaterials.9.03580

[53] R.Masel, Principles of Adsorption and Reaction on Solid Surfaces, Chapter 1, Wiley, 1996, ISBN: 978-0-471-30392-3

[54] S.S.Hars, H.R.Sharma1, J.A.Smerdon, T.P.Yadav, A.Al-Mahboob1, J.Ledieu, V.Fournée, R.Tamura, R. McGrath, Surface structure of the Ag-In-(rare earth) complex intermetallics, Physical Review B, Vol 93, 2016, DOI: https://doi.org/10.1103/PhysRevB.93.205428

[55] S.Coates, K.Nozawa, M.Fukami, K.Inagaki, M.Shimoda R.McGrath, H.R.Sharma, R.Tamura, Atomic structure of the (111) surface of the antiferromagnetic 1/1 Au-Al-Tb approximant, Physical Review B, Vol 102, 2020, DOI: https://doi.org/10.1103/PhysRevB.102.235419

[56] I.Buganski, R.Strzalka, J.Wolny, The physical space model of the Tsai-type quasi-crystal, Acta-Cryst B, 2024, DOI: https://doi.org/10.1107/S2052520624000763

[57] C.Cui , P.J.Nugent, M.Shimoda, J.Ledieu, V.Fournée, A.P.Tsai, R.McGrath, H.R.Sharma, The atomic structure of the threefold surface of the icosahedral Ag-In-Yb quasicrystal, J Phys Condensed Matter, 2012, DOI:10.1088/0953-8984/24/44/445011 (cited 3 times previously)

[58] V.Yurov, A.N.Kilmov, Correction of drift and slope distortions in STM image and scanner calibration, Surface and Interface Analysis, Vol 22, 1994, DOI: https://doi.org/10.1002/sia.740220121

[59] & [60] & [66] I.Hughes, T.Hase, Measurements And Their Uncertainties: A practical guide to modern error analysis, Chapter 4, Oxford University Press, 2010, ISBN: 9780199566334

[61] D.Freedman, P.Diaconis, On the histogram as a density estimator:L 2 theory, Zeitschrift für Wahrscheinlichkeitstheorie und Verwandte Gebiete, Vol 57, 1981, DOI: https://doi.org/10.1007/BF01025868

[62] I.Hughes, T.Hase, Measurements And Their Uncertainties: A practical guide to modern error analysis, Chapter 6, Oxford University Press, 2010, ISBN: 9780199566334

[63] & [64] & [65] H.H.Brongersmaa, M.Draxlerc, M.de Riddera, P.Bauerc, Surface composition analysis by low-energy ion scattering, Sections 6 and 7, Surface Science Reports, Vol 62, 2007, DOI: 10.1016/j.surfrep.2006.12.002

[67] M.Tsukada, K.Kobayashi, N.Isshiki, H.Kageshima, First-principles theory of scanning tunneling microscopy, Surface Science Reports, Vol 13, 1991, DOI: https://doi.org/10.1016/0167-5729(91)90006-J

[68] K.Choudhary, K.F.Garrity, C.Camp, S.V.Kalinin, R.Vasudevan, M.Ziatdinov, F.Tavazza ,Computational scanning tunneling microscope image database, Scientific Data, vol 8, DOI: https://doi.org/10.1038/s41597-021-00824-y

[69] I.Hughes, C.S.Adams, Optics f2f: From Fourier to Fresnel, Oxford University Press, 2018, ISBN: 9780198786788

[70] J.W.Arblaster, Selected Values of the Crystallographic Properties of the Elements, ASM International, 2018, Acessed online: 12/03/26, E-ISBN: 978-1-62708-155-9

[71] R. Knott, Personal Website Lectures: Binet's Formula and the Fibonacci Numbers, https://r-knott.surrey.ac.uk/fibonacci/fibformula.html, Accessed: 24/04/26

List of Figures

1 Example of a (111) plane over-layed onto cubic unit cell with basis vectors a_i. The x, y and z intercepts are all at unity relative to the lattice vectors hence taking their reciprocal and finding the integer ratio we get (111) as our Miller indices. [Kittel [13]] 3

2 2d illustration of the cut and project method our orthogonal subset is to be the line y=mx with the projection region W highlighted in orange. [A.Jagannathan, 2020 5

3 Decomposed Tsai cluster showing the progression of shells from smallest to largest. Third shell is composed of Yb. [S.Coates, 2019] 6

4 Diagram of the STM UHV chamber contained within the SSRC lab. [Sam Coates, 2019] 7

5 Vesta structural model showing Yb (turquoise) and cluster centres (red). In the figure, the page portrait direction is the (111) direction. Clear plane progressions can be seen between Yb subplanes. 11
6 Left hand image: Histogram showing measured step heats with Gaussian fit overlayed. Legend format: (Mean, Standard deviation). We can see 4 clear Poisson curves with high sample-size related noise, Right Hand image: Large scale STM image from our dataset showing clear terrace transitions one is labelled using a line profile. 13
7 Vesta image showing section of bulk structure oriented along (111) direction to show plane progression. Top image is a magnified C plane highlighting C subplane progressions. 14
8 I) Large scale image showing STM surface after cleaning along with clear motifs. II) Magnified section of I) showing motifs with greater resolution. Several common motifs can be seen with the image mostly being spanned by regular triangular arrays of atoms. III) Fourier transform of the STM image showing hexagonal motif symmetry. IV) High resolution image of regular triangle motif (A) with atomic distance and internal angle labelled. A-D) Identified surface motifs with names labelled. 15
9 A) Unaltered Vesta image of plane C1 with (111) direction pointing into page. B) Overlay of rough motif shapes and sizes onto same C1 plane. C) Example of similar motif to observed Vesta model matching shape, size and orientation. A rhombus is overlayed to allow better image comparison. 16
10 A) Vesta image of C2 plane showing regular arrays of Yb (turquoise) and In (Pink) triangles. B) Computational modelling of same Vesta planes showing uniform brightness equilateral triangles. C) Comparison STM image with matching array of regular triangles of similar size. 17
11 Overall this figure compares A and B motifs to show similarity under STM simulation. A) A1 subplane simulation showing regular triangle Motifs. B) B2 plane simulation showing similarly orientated triangle motifs. C) Comparison STM example showing internal triangles as too low resolution to distinguish A and B planes. D-F) Same structure as A-C) for different motif. ie D shows A2 simulation and E shows B3 simulation. F) shows matching orientation for macro scale motifs 18

12 Left-hand plot shows composition vs dose for sputter cycle 2. We can see an initial In richness and Ag depletion which rapidly stabilises as we reach the bulk. Right-hand plot shows sputter cycle 3 and demonstrates a similar trend. The peak compositions correspond to the post-annealing (ie surface) composition with the first few sputtering doses removing accumulated oxides from the 2 hour post annealing cooling period. 19
13 Three fold comparison figure showing the arial density of species throughout the strucuture. The Z coordinate start values are arbitrary with data being taken from a 80 Å section (ie showing all 4 subplanes). The first graph is a comparison of Ag and Yb, the second (middle) is of In and Yb and the right hand plot is Yb. We have included the third plot to allow the reader to identify the subplanes clearly, the group of 4 peaks is plane C from which others can be derived. Note the x scale on the Yb only plot is adjusted for clarity and is not the same as used in the other plots. 22
14 Labelled diagram showing cluster centres (red circles). The planes are labelled for clarity with 2d being the total cluster height hence we see A and B are separated by one cluster width. The low density plane between A and B is also shown to allow cluster cleavage counts to be made. 23
15 Labelled diagram showing glue atoms (large turquoise circles), cluster centres (red circles), and Yb cluster atoms (small turquoise dots). A c plane is labelled showing it to be the only plane with glue atoms with the highest density located within the middle 2 subplanes (ie C2 and C3). 24
16 Yb clusters composing single unit cell. Image is taken looking along the x axis hence we can see 4 corner clusters and the 8 internal clusters within a diamond pattern. xii
17 Yb clusters composing single unit cell. Image is taken looking along the y=x direction hence we can see all 8 corner clusters and the 8 internal clusters within a diamond pattern. xiii
18 Yb clusters composing single unit cell. Image is taken looking along the (111) direction hence we can see all 8 corner clusters and the 8 internal clusters. We can see the hexagonal symmetry present within the structure relating to the decomposition of the 6D parent space. xiii
19 A) Raw STM image without FFT correction, score marks can be seen from tip drift. B) Fourier space rendition of STM image in A. We can see bright spots corresponding to high frequency patterns. Some noise is seen in the diffuse specles surrounding the hexagonal block. C) Fourier cleaned version of A all scoring has been removed leaving clear motifs xiv
20 Drift corrected STM image (from figure 19) showing corrected hexagonal symmetry. xiv

21 A) Original STM image with no colour corrections or changes from base WSxM presets. B) Same STM image with contrast increased to clarify array of triangle motifs. xv
22 A) Is a magnified STM image showing triangular large motifs covering the top subplane. B) The same STM image with a line profile drawn coinciding with 6 atoms ie 3 triangle motifs. C) The height profile corresponding to the line drawn across image B. We can see peaks at high LDOS/bright regions and troughs corresponding to the gaps between these regions. xvi
23 A) Example STM image with black square drawn to highlight measurement section when using height histogram. B) Image of region highlighted in A showing step transition. xviii
24 Height histogram corresponding to magnified image B in figure 23. We see two rough Poisson curves with defect related noise creating spread around means. The distance between the two peaks (means) is our step height which is around 5.4 Å. xix
25 A) Shows magnified image of STM profile. A line profile is drawn from the tight binding subplane to the uniform triangle subplane. B) This shows the 1d line profile from image A) going from right to left. We can see that the tight bound triangles are located at a level approximately 1 Å higher than the uniform triangles confirming the suspected order of progression. xxi
26 A) Shows magnified image of STM profile. A line profile is drawn from the uniform triangle subplane to the regular large triangle subplane. B) This shows the 1d line profile from image A) going from right to left. We can see that the uniform triangles are located at a level approximately 1.5 Å lower than the regular triangles confirming the suspected order of progression. Additionally from this we can suggest that the order is regular triangles, tight triangles then uniform triangles indicating that this is a B subplane or alternatively a C subplane. Due to the difficulty in differentiating C planes from A and B no definitive plane identification can be made from the figures. xxii
27 Plot showing bin centres as red crosses (data points) and bin count uncertainty. A two Gaussian model is fitted to the data points shown in green. xxiv
28 Plot showing bin centres as red crosses (data points) and bin count uncertainty. A Three Gaussian model is fitted to the data points shown in green. xxv
29 Plot showing bin centres as red crosses (data points) and bin count uncertainty. A Six Gaussian model is fitted to the data points shown in green. We can see significant distortion of model towards the low uncertainty middle section with the model heavily coinciding with these zero points. This high fit weighting distorts the model making best fits highly inaccurate. xxv

30 Histogram of Step-heights with bin uncertainty added. The largest bin undeflow or overflow is taken as the uncertainty hence the equally sized plus and minus error bars. xxvi
31 Unfitted Spectra taken from Sputter round 3. We can see 3 peaks with Ag being the first peak on the left, In the middle peak and Yb the lower right hand peak. The Ag and In peaks are slightly overlapped due to their similar energy loss upon reflection. xxviii
32 Same spectra from Sputter round 3 with 3 Gaussians manually fitted. We can see that the baseline is much higher on the right hand side with heavily reflected ions having less energy. Hence, we can see that without baseline adjustment our Ag and In counts would be artificially high. xxix
33 Final baseline adjusted spectra removing ghost counts from unequal baseline. . . xxix
34 A) Shows a computer simulation of C2 plane section showing mixture of tight irregular triangles and diffuse spiral. B) Is a rendition of the 2D plane with Yb atoms in green, In atoms in blue. C) STM image showing similar motifs to those seen in simulation. xli
35 A) A 2D simulation of C2 plane with Ag in red, In in blue and Yb in green. B) Shows a computer simulation of C2 from higher dz point. This time the simulation shows the top regular triangles which shadow the triangles seen in figure (32). C) Matching STM motif with similar size to expression of upper C2 plane under simulation. xlii
36 A) A computer simulation of A2 plane showing array of uniform triangles composed of 3 smaller triangles B) A 2D simulation of A2 plane with Ag in red, In in blue and Yb in green. C) Similar triangle motifs with 3 component triangles matching those seen in the simulation. xlii
37 A) A 2D simulation of C3 plane with Ag in red, In in blue and Yb in green. B) A computer simulation of the corresponding C3 plane which demonstrates tight irregular triangles in a periodic array. C) A similar array of tight irregular triangles seen in STM image. The LDOS is slightly more diffuse than our model likely due to hybridisation of electron densities between closely packed atom arrangements. xliii
38 A) A 2D simulation of C1 plane with Ag in red, In in blue and Yb in green. B) Computer simulation of C1 plane showing uniform triangles. C) STM image showing similar patterns. Our model slightly overestimates LDOS contribution which may explain why smaller triangle composition isn't identified. xliii
39 Vesta image showing planes with 111 vector direction pointing up page plane. In the image only Yb atoms are shown (turquoise) and cluster centres (red). This was done for clarity purposes. xliv

40 Isolated Vesta image of C plane with 4 subplanes shown. In the image only Yb atoms are shown (turquoise) and cluster centres (red). This was done for clarity purposes. xliv
41 Left hand image is a Vesta image of C2 plane only showing Yb (blue) and cluster centres (red). Right hand image is the same C2 plane but now including In (purple) and Ag (silver). We can see very dense arrays of triangles in the right hand image. xlv
42 Left hand image is Vesta image with rough overlay of motif polyhedra. We can see that the Yb only LDOS consists of large irregular triangles. The right hand image shows a possible match to the Yb only fit with similar tight irregular triangles in array. xlv
43 Apparatus used for STM analysis xlvii
44 Gantt chart showing planned schedule of work, analysis and write-up xlix
45 Example of Penrose tiling on the left next to approximant to that tiling on the right. l
46 Example of STM image showing structure of lead surface. li

List of Tables

1 mean motif sizes and angles 15
2 Table showing composition peaks for each sputter cycle along side bulk composition. 19
3 Table showing best match to indium rich surface planes. Due to space the remaining matches are listed within Appendix C. 19
4 Table of compiled motif measurements and uncertainties with all units in nm . . xvii
5 Table of compiled step-height measurements with all values given in Å xx
6 Table comparing number of Gaussians fitted to best derived reduced chi-squared xxiv
7 Table listing LEIS composition change with dose applied for sputtering round 2. xxxi
8 Table listing LEIS composition change with dose applied for sputtering round 3. xxxiii
9 Table showing C2 composition match compared to the LEIS data. Deviation is explained through high LEIS uncertainty. xxxviii

7 Appendices

In this section we will provide any extra or required material that we believe may aid the reader in understanding and interpreting our findings. Additionally, much of the raw data can be found in this section from which independent reproducibility studies can be conducted.

7.1 Fibonacci Sequence

Due to its utility within Tsai cluster based system we will briefly describe the Fibonacci sequence. The Fibonacci sequence is a recursive series starting at 1 with derives consecutive terms by adding the previous two terms. For instance, starting at 1 the first few terms of the sequence is given by:

$$F = 1, 1, 2, 3, 5, 8, ... \tag{5}$$

Extending this, we may derive any term with the Fibonacci sequence using Binet's Formula:

$$F = \frac{\phi^n - (1-\phi)^n}{\sqrt{5}} \tag{6}$$

where ϕ or τ as it is referred to in the text is the golden ratio. Equally if we know two consecutive terms in the Fibonacci sequence we can use these to provide an approximation for ϕ by taking their quotient with:

$$\lim_{n\to\infty} \frac{F_n}{F_{n-1}} = \phi \tag{7}$$

[71].

7.2 Structure Visualisation

To some degree the model presented is quite hard to visualise from the text alone. Hence, as an aid to the reader several labelled figures of the structure are given here:

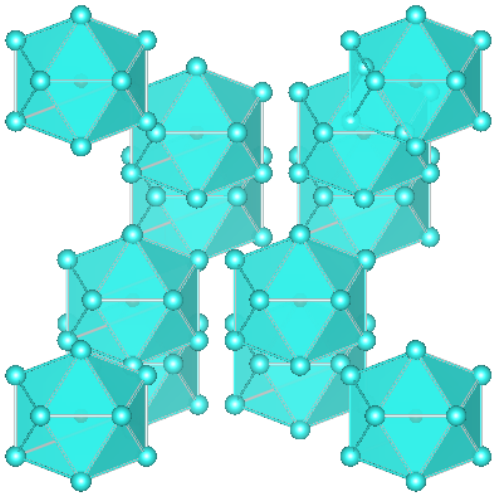


Figure 16: Yb clusters composing single unit cell. Image is taken looking along the x axis hence we can see 4 corner clusters and the 8 internal clusters within a diamond pattern.

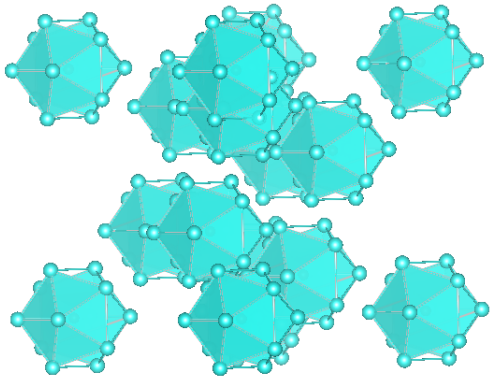


Figure 17: Yb clusters composing single unit cell. Image is taken looking along the y=x direction hence we can see all 8 corner clusters and the 8 internal clusters within a diamond pattern.

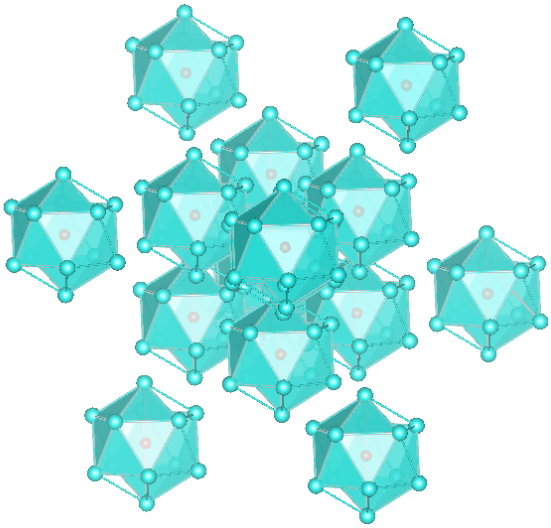


Figure 18: Yb clusters composing single unit cell. Image is taken looking along the (111) direction hence we can see all 8 corner clusters and the 8 internal clusters. We can see the hexagonal symmetry present within the structure relating to the decomposition of the 6D parent space.

7.3 Appendix A - STM Data Processing and Measurement Methods

7.3.1 STM Image Processing

Before motif or step defect measurements could be taken from the 130 STM images they required cleaning. This was done to remove isolated defects such as tip line scores, missed scanning sections or adatoms. Within WSxM the fast Fourier transform tool was used to perform frequency decomposition and remove these isolated defects. This tool shows the frequency or Fourier space decomposition of the image signal allowing isolation of bright signals corresponding to repeated or high frequency features.

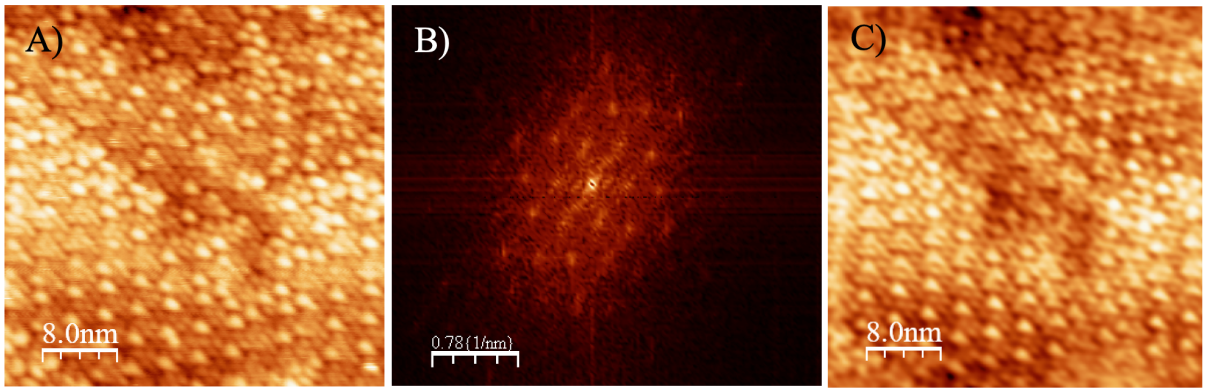


Figure 19: A) Raw STM image without FFT correction, score marks can be seen from tip drift. B) Fourier space rendition of STM image in A. We can see bright spots corresponding to high frequency patterns. Some noise is seen in the diffuse specles surrounding the hexagonal block. C) Fourier cleaned version of A all scoring has been removed leaving clear motifs

Once these features are isolated, the reconstructed image only shows the repeated motifs. These motifs are still distorted due to slope and drift effects arising from imperfections in the control of the piezoelectric tip drivers [58]. These distortions are identified within the Fourier transform of the image manifesting as drift in the hexagonal (6-fold) symmetry present within the approximant.

We corrected this manually by first identifying that the large regular triangle motifs should theoretically form regular hexagons based on the Vesta structure. The images were then imported into Inkscape and manually manipulated until the symmetry of these hexagons was restored. The Fourier transform was then retaken to confirm that the distortion had be rectified allowing use of the images to make motif measurements.

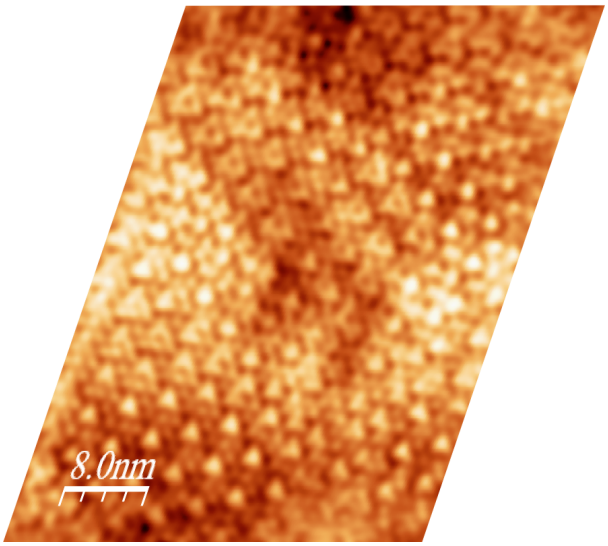


Figure 20: Drift corrected STM image (from figure 19) showing corrected hexagonal symmetry.

Further aesthetic corrections were made when identifying arrays of motifs and making measurements. These include making plane corrections using WSxM to level the surface of the image allowing clear identification of motif boundaries and sizes. Additionally, the colours and contrast were adjusted to clarify the boundary of motifs when making measurements and when preparing figures. This was done to better display motifs of limited contrast to the background LDOS signal. Inclusion of all adjusted images would be impractical, however, a figure example is given above of the outlined cleaning process. Requests for access to the raw and cleaned images can be made to the SSRC Liverpool.

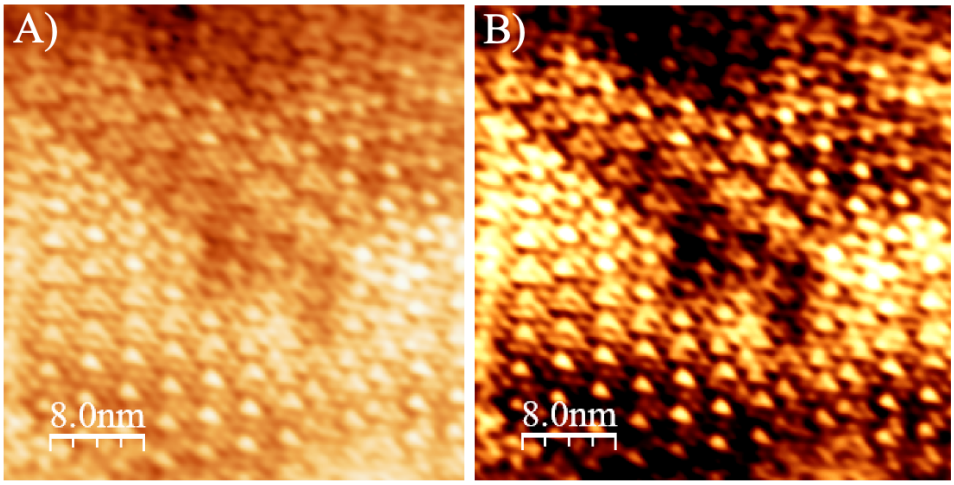


Figure 21: A) Original STM image with no colour corrections or changes from base WSxM presets. B) Same STM image with contrast increased to clarify array of triangle motifs.

7.3.2 Motif Measurements

The measurement of motifs was done in WSxM. First, the cleaned images were visually inspected to identify clear motif regions with sufficient size to allow measurement. Once regions of sufficient size were identified, the line profile tool was used to measure the size of the motifs. This was done by drawing a line along the repeating motifs starting before the motif and ending afterwards to prevent elision of motif data. Due to the stochastic nature of the images, the normal limit of 5 collinear motifs was adjusted to 3 to increase the number of available measurement locations.

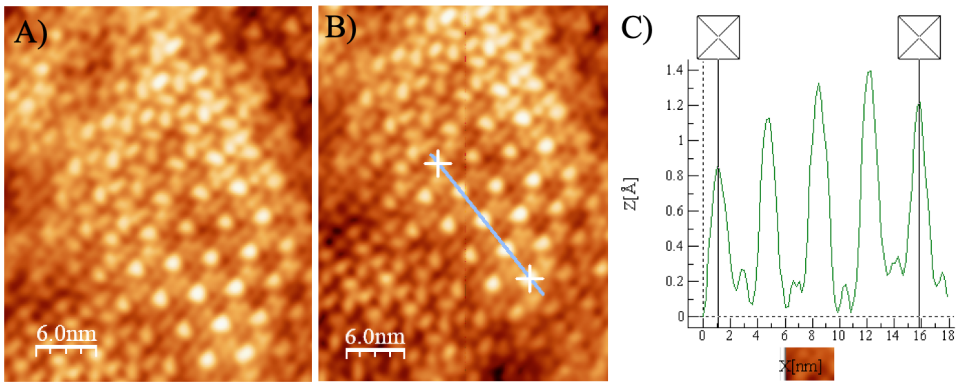


Figure 22: A) Is a magnified STM image showing triangular large motifs covering the top subplane. B) The same STM image with a line profile drawn coinciding with 6 atoms ie 3 triangle motifs. C) The height profile corresponding to the line drawn across image B. We can see peaks at high LDOS/bright regions and troughs corresponding to the gaps between these regions.

The line profile tool produces a 1d continuous height profile along the selected line. The peaks correspond to the locations of surface atom arrangements (bright regions). By using the inbuilt profile measurement tool, the distance between all the motifs was measured by taking the difference between the location of the first peak and the last. The location of the peak was identified visually hence, the uncertainty in the distance measurements was taken as the standard deviation of the Gaussian peaks. Consequently, the overall uncertainty of the entire profile was taken as the sum of the standard deviation of the first and last peaks. The motif size was then derived by dividing the total distance by the number of peaks minus one to account for the initial peak. The total uncertainty was similarly divided by this number in line with standard error propagation.

For the irregular triangles, in which no clear none-extended peaks could be identified, the line profile was drawn along the rough corners of the motifs. The position of the triangle edges was determined visually using the position tool to identify the section of the image which was being measured. Due to the visual nature of the size determination the uncertainty in the diffuse triangles was taken as the cross hair width plus the peak deviation.

A list of all the motif measurements made is provided in the table below. The mean motif width was calculated from each of the measurements with the total uncertainty being derived by the standard quadratic addition formula:

$$\alpha_z = |Z| \sqrt{\sum \frac{\alpha_n^2}{Z_n^2}} \tag{8}$$

Where α_n is the uncertainty in the nth motif measurement, Z_n is the nth motif size, $|Z|$ is the motif mean size, and α_z is our mean uncertainty [59].

Regular Triangles (nm)	Irregular spiral (nm)	Tight Triangle (nm)	Uniform Triangle (nm)
3.55 ± 0.05	1.98 ± 0.03	3.4 ± 0.10	2.2 ± 0.30
3.59 ± 0.06	1.92 ± 0.03	3.5 ± 0.10	2.4 ± 0.20
3.51 ± 0.05	1.95 ± 0.04	3.2 ± 0.20	2.2 ± 0.20
3.68 ± 0.07	2.04 ± 0.03	3.4 ± 0.10	2.1 ± 0.10
3.65 ± 0.04	2.05 ± 0.04	3.6 ± 0.10	2.4 ± 0.30
3.50 ± 0.03	1.92 ± 0.05	3.7 ± 0.10	2.2 ± 0.20
3.49 ± 0.05	1.68 ± 0.05	3.5 ± 0.20	2.3 ± 0.10
3.68 ± 0.05	1.79 ± 0.03	3.5 ± 0.10	2.1 ± 0.20
3.75 ± 0.05	2.03 ± 0.03	3.1 ± 0.20	2.1 ± 0.20
3.89 ± 0.07	1.77 ± 0.03	3.3 ± 0.10	
3.55 ± 0.05	1.84 ± 0.04	3.6 ± 0.30	
3.45 ± 0.06	1.66 ± 0.03	3.7 ± 0.10	
3.61 ± 0.05	1.64 ± 0.10	3.8 ± 0.10	
3.81 ± 0.05	1.93 ± 0.08	3.4 ± 0.10	
3.53 ± 0.04	1.68 ± 0.04	3.500 ± 0.10	
3.51 ± 0.04	1.97 ± 0.05	3.4 ± 0.10	
3.42 ± 0.06		3.01 ± 0.20	
3.56 ± 0.09		3.6 ± 0.10	
		3.71 ± 0.10	
		3.65 ± 0.20	
		3.25 ± 0.10	

Table 4: Table of compiled motif measurements and uncertainties with all units in nm

7.3.3 Step-Height Measurement

The 10 large scale images taken all contained multiple step defects allowing measurement of a wide range of plane terminations. To prevent disproportionate representation of specific, clear step defects within the histogram each plane termination was measured 3 times from 3 different locations along the terrace. The mean step-height was then calculated from these 9 measurements and added to the table used within our histogram (Table 4). The uncertainty in this was taken simply as the standard error calculated via the following:

$$\alpha = \frac{\sigma}{\sqrt{N}} \tag{9}$$

Where α is the standard error, σ is the standard deviation, and N is the sample size [60].

The measurement procedure itself was quite simple. We first took a thin magnified image of the terrace transition and used the height histogram feature in WSxM to create a visual of all the heights present in the image. For a single terrace transition, with standard noise from terrace defects, this appeared as two Poisson curves. Taking the difference between the mean of these two poisson curves, using the WSxM measurement curser, then gave the step-height. As described, the location and orientation was then changed and the measurement re-performed until we had 9 measurements for the terrace transition.

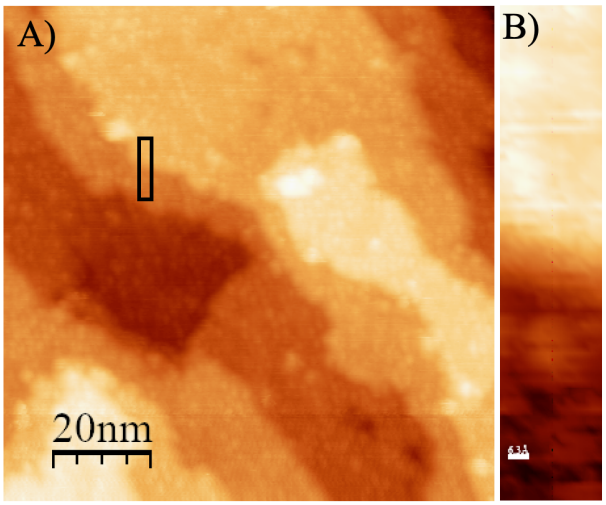


Figure 23: A) Example STM image with black square drawn to highlight measurement section when using height histogram. B) Image of region highlighted in A showing step transition.

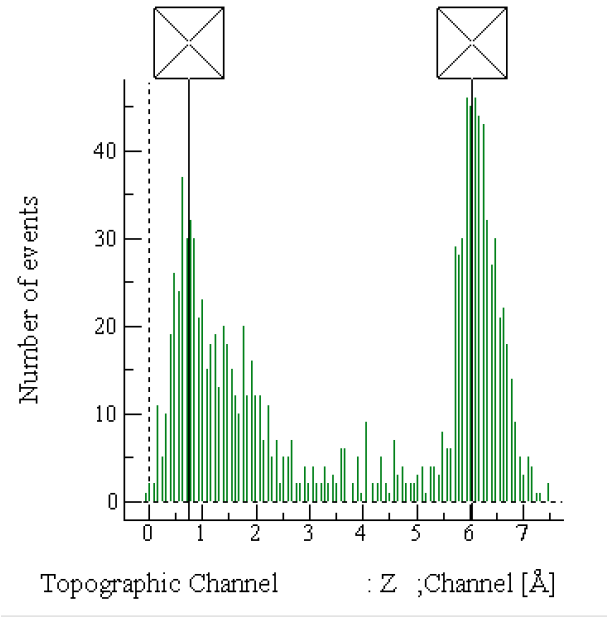


Figure 24: Height histogram corresponding to magnified image B in figure 23. We see two rough Poisson curves with defect related noise creating spread around means. The distance between the two peaks (means) is our step height which is around 5.4 Å.

121 of these procedures were completed over all the terraces until we had a relatively complete image of the commonality and size of the terrace transitions. These were then plotted as a histogram, the analysis of which is discussed in the next appendix. A table of all 121 measurements and their uncertainties is included below.

Step-heights	Step-heights	Step-heights	Step-heights	Step-heights	Step-heights
4.57 ± 0.05	4.4 ± 0.1	4.42 ± 0.07	4.8 ± 0.2	4.38 ± 0.08	4.36 ± 0.08
4.5 ± 0.1	4.5 ± 0.1	4.6 ± 0.1	4.61 ± 0.07	4.1 ± 0.1	4.22 ± 0.09
4.49 ± 0.07	4.4 ± 0.1	4.32 ± 0.05	4.6 ± 0.2	4.49 ± 0.07	4.5 ± 0.2
4.66 ± 0.06	4.6 ± 0.2	4.96 ± 0.08	4.30 ± 0.04	4.7 ± 0.1	4.39 ± 0.08
4.05 ± 0.07	4.42 ± 0.05	4.31 ± 0.06	4.16 ± 0.09	3.67 ± 0.04	3.8 ± 0.1
3.83 ± 0.09	3.51 ± 0.03	3.96 ± 0.05	4.04 ± 0.07	3.19 ± 0.06	3.50 ± 0.2
3.96 ± 0.08	3.85 ± 0.06	3.7 ± 0.1	3.97 ± 0.05	3.68 ± 0.07	3.43 ± 0.07
3.4 ± 0.1	3.5 ± 0.1	3.3 ± 0.2	5.03 ± 0.08	4.97 ± 0.09	5.3 ± 0.3
5.54 ± 0.03	5.65 ± 0.05	5.2 ± 0.1	5.54 ± 0.05	5.85 ± 0.08	5.45 ± 0.06
5.3 ± 0.2	5.57 ± 0.08	5.90 ± 0.08	4.35 ± 0.05	5.49 ± 0.04	4.52 ± 0.07
3.57 ± 0.08	4.39 ± 0.09	4.8 ± 0.2	5.33 ± 0.09	5.0 ± 0.3	4.55 ± 0.08
4.63 ± 0.05	4.44 ± 0.07	3.58 ± 0.04	3.98 ± 0.09	4.68 ± 0.06	5.39 ± 0.07
4.1 ± 0.1	3.8 ± 0.1	4.13 ± 0.08	4.7 ± 0.2	3.52 ± 0.05	4.4 ± 0.08
3.8 ± 0.3	4.4 ± 0.2	4.59 ± 0.09	3.80 ± 0.1	5.05 ± 0.07	4.2 ± 0.1
5.30 ± 0.06	4.56 ± 0.08	5.86 ± 0.05	4.92 ± 0.09	4.3 ± 0.2	4.12 ± 0.04
5.85 ± 0.03	5.6 ± 0.1	5.57 ± 0.09	4.3 ± 0.2	3.64 ± 0.05	3.27 ± 0.07
4.34 ± 0.08	3.76 ± 0.05	3.53 ± 0.07	3.62 ± 0.04	3.4 ± 0.2	0.80 ± 0.02
0.78 ± 0.01	3.9 ± 0.1	4.48 ± 0.08	3.5 ± 0.1	4.45 ± 0.08	3.73 ± 0.04
1.23 ± 0.01	0.81 ± 0.03	1.43 ± 0.01	1.23 ± 0.03	1.61 ± 0.02	0.91 ± 0.02
1.07 ± 0.01	1.18 ± 0.05	1.15 ± 0.04	0.95 ± 0.03	1.08 ± 0.03	1.56 ± 0.02
1.10 ± 0.04					

Table 5: Table of compiled step-height measurements with all values given in Å

7.3.4 Variation in A/B motif ordering

As mentioned in the main body of the report, A and B planes are mirror images of each-other with inverse ordering. We expect therefore to see a different ordering of motifs when comparing A and B planes reflecting the different subplane order.

From simulations we expect A subplanes to present as A1 to A2 which manifests by the local ordering: Tight irregular triangles - Regular large triangles - uniform triangles. Meanwhile for B, given that we're seeing B3 to B2, we expect the following ordering: Regular large triangles - Tight irregular triangles - uniform triangles. (The first motif listed is the top presenting motif.)

This ordering was confirmed using image height analysis of the motifs. We drew line profiles crossing multiple subplanes to gauge their height order. This was done over the 3 small scale images with A to B step transitions shown. This produced clear, continuous profiles showing

our predicted ordering as well as confirming the larger step divide between the uniform triangles and middle motif in plane B (1Å compared to 0.8Å).

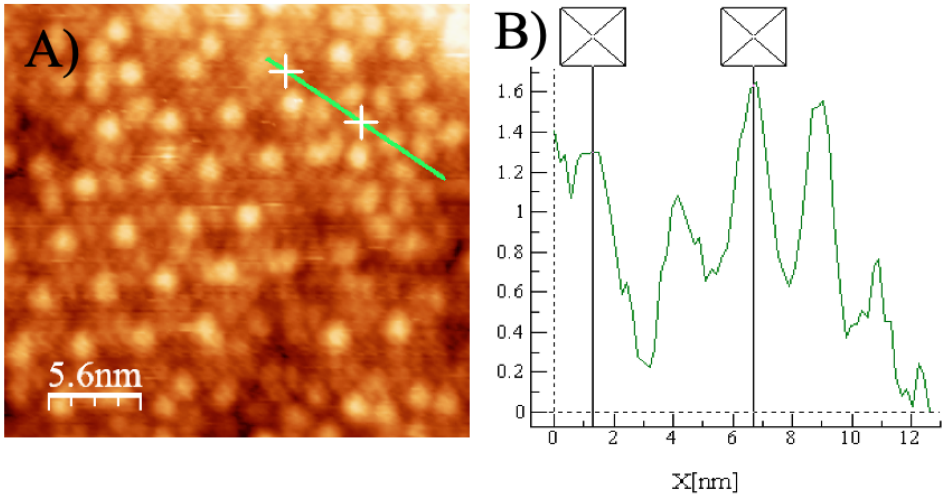


Figure 25: A) Shows magnified image of STM profile. A line profile is drawn from the tight binding subplane to the uniform triangle subplane. B) This shows the 1d line profile from image A) going from right to left. We can see that the tight bound triangles are located at a level approximately 1 Å higher than the uniform triangles confirming the suspected order of progression.

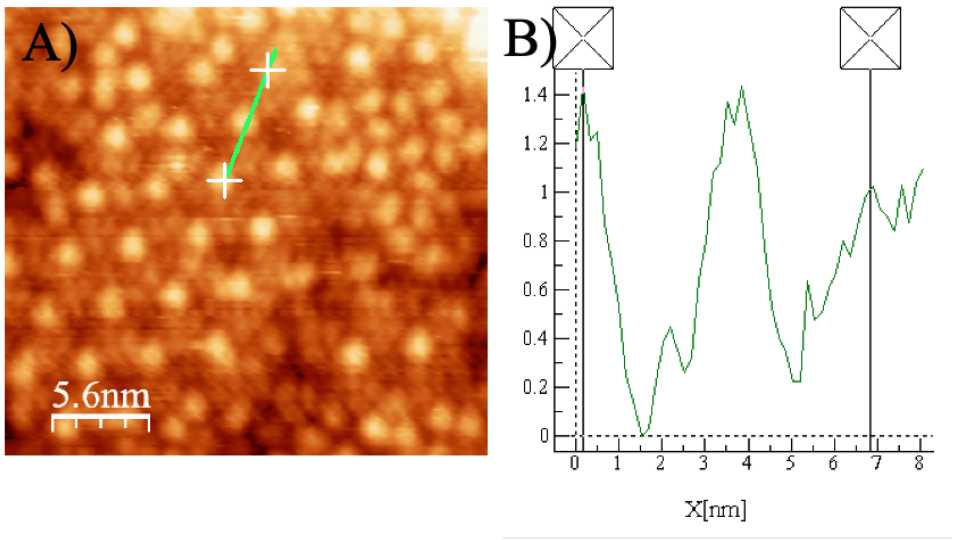


Figure 26: A) Shows magnified image of STM profile. A line profile is drawn from the uniform triangle subplane to the regular large triangle subplane. B) This shows the 1d line profile from image A) going from right to left. We can see that the uniform triangles are located at a level approximately 1.5 Å lower than the regular triangles confirming the suspected order of progression. Additionally from this we can suggest that the order is regular triangles, tight triangles then uniform triangles indicating that this is a B subplane or alternatively a C subplane. Due to the difficulty in differentiating C planes from A and B no definitive plane identification can be made from the figures.

It is to be noted that, although several profiles were sampled, only 3 images were suitable for testing. Hence, no exact transition sizes can be given due to our limited STM resolution at less than 1 Å scales and the high influence of defects at such small sample sizes.

7.4 Appendix B - Step Height Analysis and Gaussian Fitting

7.4.1 Bin Fitting

Having recorded 121 step-heights, we needed a robust method in which to analyse their distribution and identify the number of step-heights present. The standard method in which this is done is by use of Histogram analysis in which step-heights are identifiable as Poisson distributions around a mean (our step-height).

In creating this Histogram the Freedman-Diaconis formula was used when determining the bin width (bin number) used:

$$W = \frac{2(IQR)}{\sqrt[3]{N}} \tag{10}$$

Where W is the bin-width, IQR is the interquartile range, and N is the number of measurements (121) [61]. This allowed us the prevent over-smoothing of less frequent step-heights preventing

their misidentification in later continuum analyses. Using this formula, we derived an ideal bin width of 0.18 nm This figure was adjusted to 0.1 nm (40 bins) which provided a clearer distribution while, still balancing the influence of random noise and over-smoothing. Finally, the plotted Histogram was normalised to show frequency density using the standard in-built mathplotlib.pyplot normalisation command.

7.4.2 Chi-squared Analysis

To allow proper fitting of Gaussians to our step-height distribution the data was converted to a continuum. This was done by taking the x coordinate as the bin centre location and the frequency density as the y coordinate. This then allowed us to use standard model optimisation code within Scipy to fit model parameters. A copy of the code used to fit the gaussian model can be found labelled within the code repository (Appendix D).

Our model used standard variation of parameters to derive optimised coefficients using the reduced chi-squared as a model fit test. The reduced chi-squared was calculated using the standard formula:

$$\chi^2 = \frac{\sum \frac{(E_i - O_i)^2}{E_I}}{\nu} \tag{11}$$

Where χ^2 is our reduced chi-squared, E_i is our ith model predicted value, O_i is ith our data value, and ν is our degrees of freedom [62].

All the models tested where of Gaussian form with the only adjusted parameter being the number of Gaussians fitted. The multiple Gaussian model took the standard form:

$$y = \sum A_i e^{-a_i(x+b_i)^2} \tag{12}$$

Where a_i, A_i, and b_i are simply optimised parameters. With i varied for each model to determine the best number of Gaussians.

We tested a series of possible models ranging from 1 Gaussian to a maximum of 7. The clear best fit identified was 4 Gaussians indicating the presence of 4 step-heights with all other models either being over fit (small chi-squared) or poor fitting (large chi-squared). For the purposes of completeness, we've included plots of some of the model fits tested along side the derived reduced chi-squared. (Note: the higher fits despite having low chi-squared were very visibly over-fitted see figure (26). The high errors when using our bin centre decomposition did contribute heavily to some of this over-fitting and strange chi-squared values at higher Gaussian fits. Hence, above 4 fitted curves the middle section with very small errors (i.e. no frequency data) did have overly high weighting leading to distorted fits.)

Gaussian number	Reduced Chi-Squared
1	4×10^5
2	44.7
3	7.36
4	5.43
5	1×10^4
6	4.43
7	7.95

Table 6: Table comparing number of Gaussians fitted to best derived reduced chi-squared

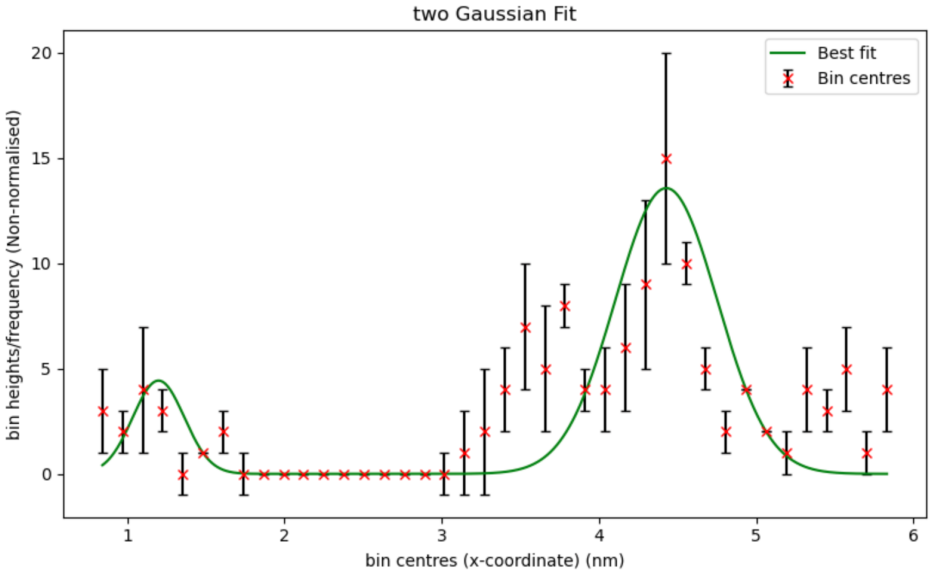


Figure 27: Plot showing bin centres as red crosses (data points) and bin count uncertainty. A two Gaussian model is fitted to the data points shown in green.

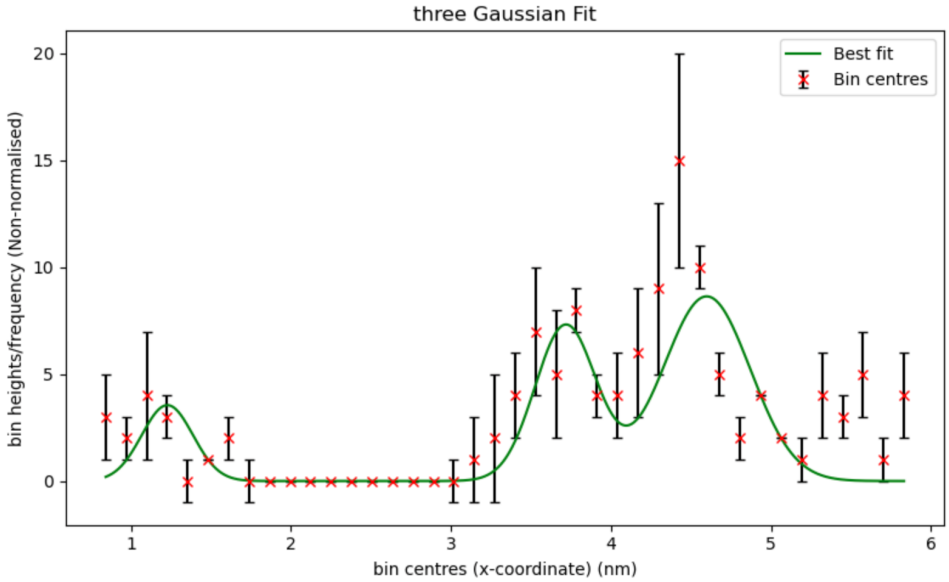


Figure 28: Plot showing bin centres as red crosses (data points) and bin count uncertainty. A Three Gaussian model is fitted to the data points shown in green.

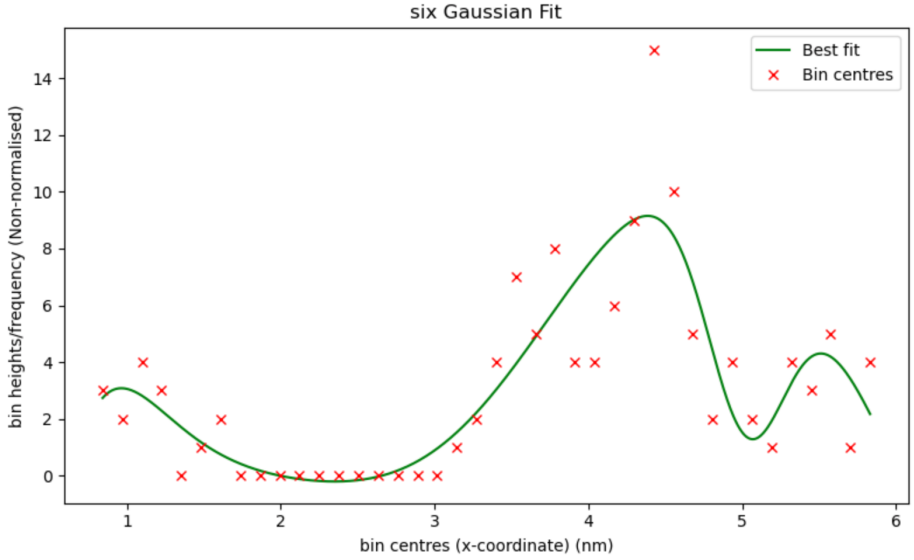


Figure 29: Plot showing bin centres as red crosses (data points) and bin count uncertainty. A Six Gaussian model is fitted to the data points shown in green. We can see significant distortion of model towards the low uncertainty middle section with the model heavily coinciding with these zero points. This high fit weighting distorts the model making best fits highly inaccurate.

7.4.3 Histogram Uncertainty

Due to clarity reasons the uncertainty in the bin counts wasn't shown graphically within the main body of the report. The bin uncertainties were calculated and used when calculating the model fit.

This was done manually by counting the number of data-points which had an uncertainty and value such that with their uncertainty added or removed would end up in the bin below or above. Hence, doing this for all the bins we arrived at a maximum and minimum bin occupancy. This was taken as the count uncertainty range. A continuum plot showing the bin centres and the uncertainty ranges on the bins is included below.

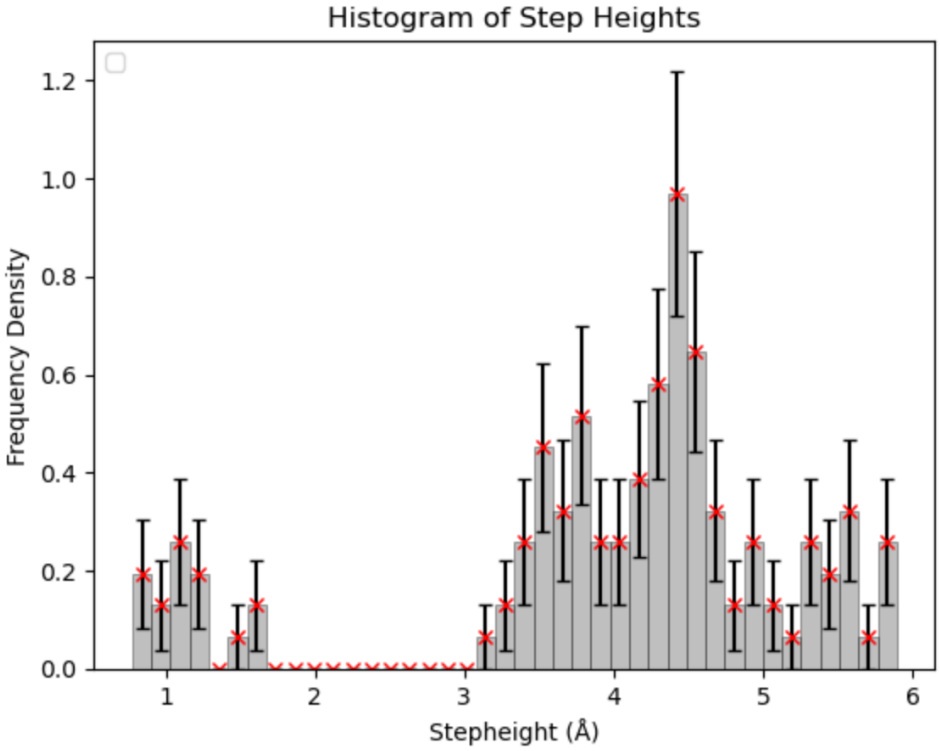


Figure 30: Histogram of Step-heights with bin uncertainty added. The largest bin undeflow or overflow is taken as the uncertainty hence the equally sized plus and minus error bars.

7.5 Appendix C - LEIS Spectra Analysis

7.5.1 LEIS Spectra fitting

Spectra fitting was completed mostly automatically using the inbuilt Ionfit software on the laboratory computer. The software was used to fit 3 Gaussians to the Spectra using model optimisation through least squares analysis. Three peaks were fitted with the understanding that only In, Yb, and Ag would be present on the surface with the influence of impurities post the first sputter cycle being limited. The reason machine optimisation was used, rather than manual fitting, was to account for the quite complex spread of ion energies. We expected both a rough spread in beam energy around 5 KeV due to machine limitations. Additionally, variation in the vibrational modes of the species may contribute to spread. Overall these lead to Doppler broadening of the peak of the order:

$$\delta z \approx \sqrt{E_0 \times E_v} \tag{13}$$

Where δz is the spectra broadening, E_0 is the machine energy broadening, and E_v is the vibrational energy of the target atom [63]. Hence, Ionfit being able to account for temperature variation and species type when fitting was chosen to be the best fitting tool. Ionfit also provides a means to account for various other sources of error such as double scattering of ions and re-ionisation. This is done through tail analysis of the spectra which represents background counts from ions going through multiple scattering and reionisation deeper into the sample. The complexity of doing this manually would be quite high which is why prebuilt tools were chosen for the spectra analysis.

In addition to this error procedure, spectra were initially visually inspected before fitting to check for bulk impurities which would present as another observed peak and thus invalidate our 3 fit optimisation. This allowed us to precisely fit Gaussians for each species present with the knowledge that no broadening effects from unknown species were elised.

As mentioned previously in the main body of the report, manual calibration was needed to remove baseline offset when fitting. This offset arises due to a mixture of effects including 'tail' effects from penetration of ions deeper into the surface (ghost counts) as well as poor initial energy calibration [64]. This adjustment was made by simply adjusting the fitted Gaussian baselines using Ionfit. This prevents us over-counting ion reflection contributions from deep within the bulk giving an inaccurately weighted surface composition. For clarity, some examples of the unfitted, fitted, and baseline adjusted Spectra are given below. There are more than 300 spectra hence we are unable to show them all, any request for data can be made to the SSRC Liverpool.

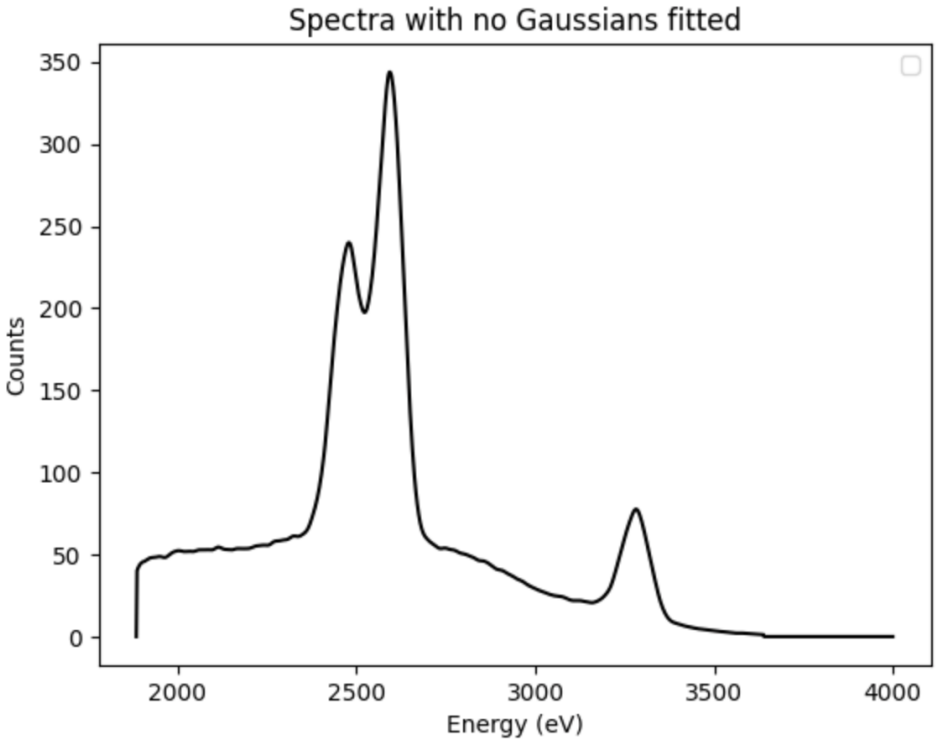


Figure 31: Unfitted Spectra taken from Sputter round 3. We can see 3 peaks with Ag being the first peak on the left, In the middle peak and Yb the lower right hand peak. The Ag and In peaks are slightly overlapped due to their similar energy loss upon reflection.

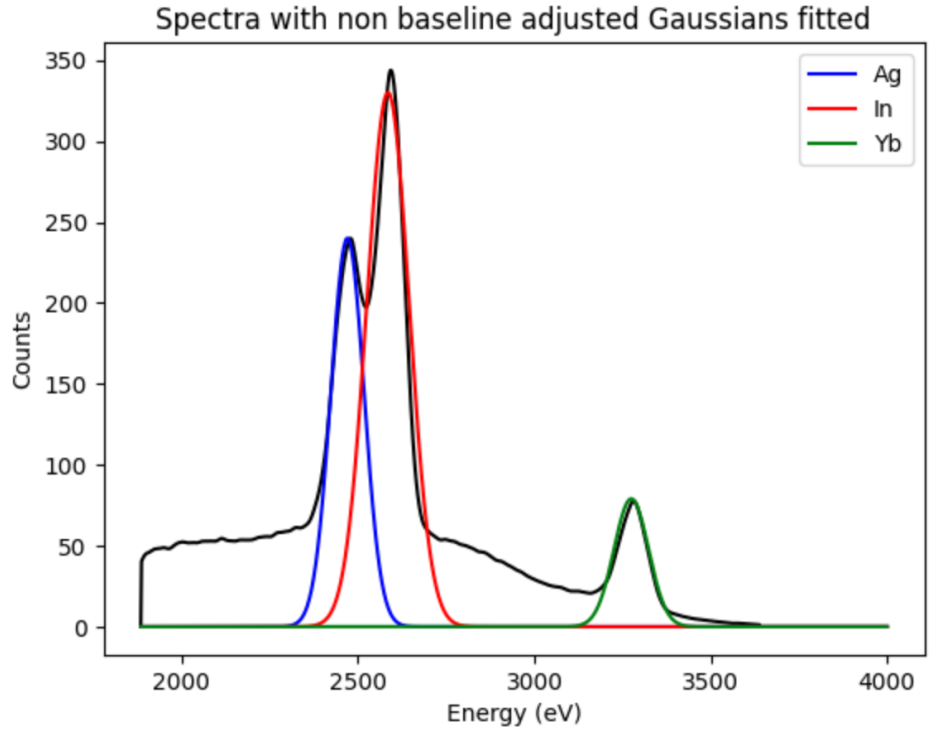


Figure 32: Same spectra from Sputter round 3 with 3 Gaussians manually fitted. We can see that the baseline is much higher on the right hand side with heavily reflected ions having less energy. Hence, we can see that without baseline adjustment our Ag and In counts would be artificially high.

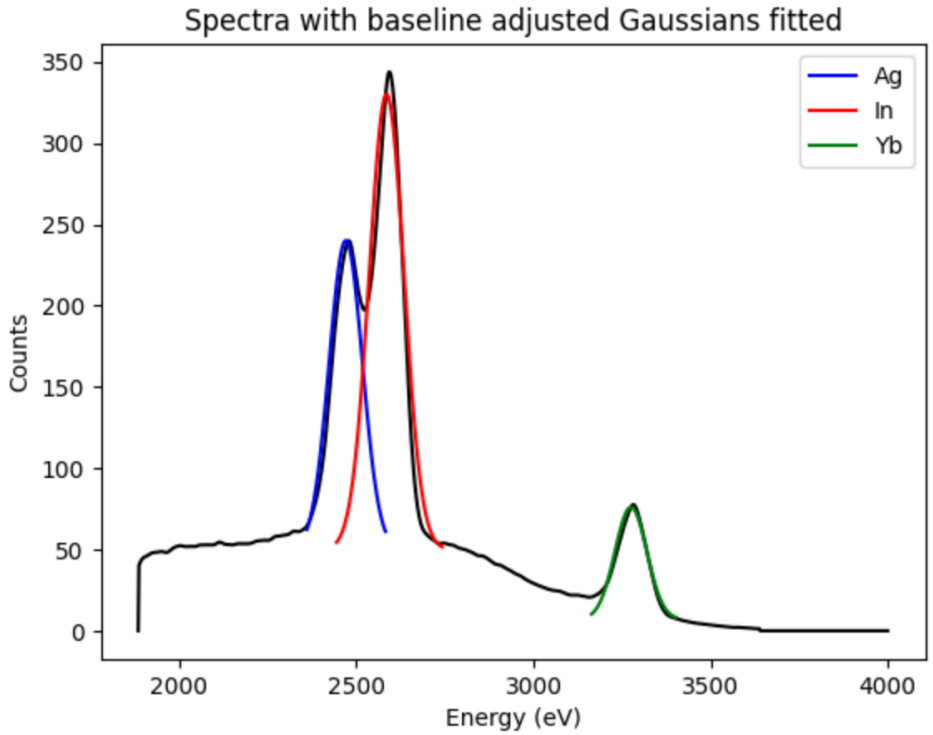


Figure 33: Final baseline adjusted spectra removing ghost counts from unequal baseline.

7.5.2 Composition Extraction

Composition extraction presents a unique challenge given that we can't assume we have one to one scattering. Some species will have smaller cross-sections and hence, scatter less frequently. We also need to know neutralisation and reionisation coefficients to work out the true counts, and ions may themselves undergo multiple scattering events before being counted. This all means that we need to convert our raw spectra counts to true counts before we can extract the composition.

Most of work is done by Ionfit itself as, it is able to use the tail signal to extract the total contribution from multiple scattering events. Hence, our extracted counts from integrating the fitted spectra were already multiple scattering event adjusted. Thus, to extract the true counts we just needed to use the following equation for the yield of backscattered ions:

$$S_i = R(\eta_i) = R(P_i + \frac{d\sigma}{d\Omega}) \tag{14}$$

Where S_i is the yield, R is a known coefficient encompassing several beam parameters, P_i is the ion fraction, and $\frac{d\sigma}{d\Omega}$ is the scattering cross section [65]. The cross sections used were those previously calculated for the quasicrystal upon which, LEIS analysis had previously been performed. Although the bulk structure differs, the relative composition ratios are still the same. We therefore, expect similar cross sections (ion stopping power). This is a major assumption and further research may benefit from verifying this assumption. The direct calculation of cross sections from the elemental references would likely represent a project in of itself. Thus, was not practical for this limited thesis.

Once, the counts had been converted to true counts using the yield equation, we then derived the composition. This was done by taking the final counts as that of the bulk. Hence, we divided all previous counts by the counts of the final dose to give the count ratios. We then multiplied these ratios by the expected bulk ratio 42Ag:42In:16Yb to give the relative composition at the surface.

The measurement uncertainty in these counts were taken using the resolution of the raw LEIS counts. For most of these this was ±10 counts. This was then propagated through the yield equation by simple multiplication. The ratio uncertainty was then taken using the standard formula for dividing two variables:

$$\alpha_{\frac{A}{B}} = |Z|\sqrt{\frac{\alpha_A^2}{A^2} + \frac{\alpha_B^2}{B^2}} \tag{15}$$

Where, in this case, A and B are simply the count numbers, and Z is the ratio value [66]. This was then multiplied by the same bulk ratio to give the composition uncertainty. This was by the far the least rigorous of our uncertainty propositions given we couldn't derive the uncertainty in the real cross sections due to us using the quasicrystal cross-sections. It should be noted the

uncertainty is likely to be higher than our calculated values therefore all LEIS data should be considered carefully before future experimentation can constrain our assumptions or clarify our true uncertainty.

A table of the compositions for each of the 2 sputtering cycles is included below:

Table 7: Table listing LEIS composition change with dose applied for sputtering round 2.

Dose (10^{15} ions cm^{-2})	Ag composition	In composition	Yb composition
0.00	28.2 ± 0.2	54.2 ± 0.7	16.95 ± 0.03
0.38	29.9 ± 0.3	55.5 ± 0.6	17.23 ± 0.03
0.77	37.7 ± 0.4	56.2 ± 0.6	16.0 ± 0.03
1.92	43.7 ± 0.4	55.2 ± 0.5	14.0 ± 0.03
3.07	44.9 ± 0.4	53.7 ± 0.4	13.9 ± 0.03
4.22	46.4 ± 0.4	51.9 ± 0.4	13.8 ± 0.03
5.37	49.8 ± 0.4	49.4 ± 0.4	12.7 ± 0.03
7.67	50.1 ± 0.4	48.3 ± 0.4	12.5 ± 0.03
9.97	51.2 ± 0.4	47.2 ± 0.4	12.8 ± 0.03
12.27	49.8 ± 0.4	46.9 ± 0.4	12.6 ± 0.03
14.57	51.0 ± 0.4	46.0 ± 0.4	12.6 ± 0.03
16.87	50.6 ± 0.4	45.6 ± 0.4	12.7 ± 0.03
19.17	50.3 ± 0.4	44.8 ± 0.3	12.6 ± 0.03
21.47	51.6 ± 0.4	44.3 ± 0.3	12.9 ± 0.03
23.77	51.1 ± 0.4	43.7 ± 0.3	12.9 ± 0.03
27.22	50.4 ± 0.4	43.7 ± 0.3	12.9 ± 0.03
30.68	50.4 ± 0.4	43.4 ± 0.3	13.2 ± 0.03
34.13	50.0 ± 0.4	43.6 ± 0.3	13.3 ± 0.03
37.58	49.9 ± 0.4	43.7 ± 0.3	13.2 ± 0.03
41.03	49.6 ± 0.4	43.4 ± 0.3	13.4 ± 0.03
44.48	48.8 ± 0.4	43.8 ± 0.3	13.5 ± 0.03
47.93	49.0 ± 0.4	43.5 ± 0.3	13.6 ± 0.03
51.38	48.5 ± 0.4	43.3 ± 0.3	13.8 ± 0.03
54.83	48.6 ± 0.4	43.3 ± 0.3	13.5 ± 0.03
58.28	48.0 ± 0.4	43.2 ± 0.3	13.9 ± 0.03
61.73	47.8 ± 0.4	43.0 ± 0.3	14.4 ± 0.03
65.18	47.6 ± 0.4	43.2 ± 0.3	14.0 ± 0.03
68.64	47.1 ± 0.4	43.2 ± 0.3	14.2 ± 0.03
72.09	46.9 ± 0.4	42.9 ± 0.3	14.2 ± 0.03
75.54	46.7 ± 0.4	43.0 ± 0.3	14.5 ± 0.03

Dose (10^{15} ions cm^{-2})	Ag composition	In composition	Yb composition
78.99	46.4 ± 0.4	42.5 ± 0.3	14.4 ± 0.03
82.44	46.1 ± 0.4	42.9 ± 0.3	14.7 ± 0.03
85.89	46.3 ± 0.4	42.7 ± 0.3	14.5 ± 0.03
89.34	45.6 ± 0.4	42.6 ± 0.3	14.7 ± 0.03
92.79	45.3 ± 0.4	42.5 ± 0.3	14.6 ± 0.03
96.24	45.9 ± 0.4	42.0 ± 0.3	14.8 ± 0.03
99.69	44.9 ± 0.4	42.7 ± 0.3	15.0 ± 0.03
103.14	44.5 ± 0.4	42.6 ± 0.3	14.8 ± 0.03
106.6	44.9 ± 0.4	42.3 ± 0.3	14.9 ± 0.03
110.05	44.4 ± 0.4	42.4 ± 0.3	15.0 ± 0.03
113.5	44.6 ± 0.4	42.4 ± 0.3	15.3 ± 0.03
116.95	43.8 ± 0.4	42.4 ± 0.3	15.2 ± 0.03
120.4	44.2 ± 0.4	42.3 ± 0.3	15.1 ± 0.03
123.85	43.8 ± 0.4	42.8 ± 0.4	15.3 ± 0.03
127.3	44.1 ± 0.4	41.9 ± 0.3	15.2 ± 0.03
130.75	43.9 ± 0.4	41.8 ± 0.3	15.3 ± 0.03
134.2	43.6 ± 0.4	41.7 ± 0.3	15.4 ± 0.03
137.65	42.7 ± 0.4	42.4 ± 0.4	15.5 ± 0.03
141.11	42.9 ± 0.4	42.0 ± 0.4	15.2 ± 0.03
144.56	42.8 ± 0.4	41.9 ± 0.3	15.3 ± 0.03
148.01	43.2 ± 0.4	41.9 ± 0.3	15.5 ± 0.03
151.46	43.1 ± 0.4	41.5 ± 0.3	15.7 ± 0.03
154.91	42.7 ± 0.4	41.6 ± 0.3	15.6 ± 0.03
158.36	42.0 ± 0.4	42.3 ± 0.4	15.5 ± 0.03
161.81	43.3 ± 0.4	41.4 ± 0.3	15.5 ± 0.03
165.26	42.7 ± 0.4	41.7 ± 0.3	15.7 ± 0.03
168.71	42.2 ± 0.4	41.7 ± 0.3	15.9 ± 0.03
172.16	42.4 ± 0.4	41.7 ± 0.4	15.8 ± 0.03
175.61	41.9 ± 0.4	41.9 ± 0.4	15.8 ± 0.03
179.07	42.2 ± 0.4	41.7 ± 0.4	15.8 ± 0.03
182.52	42.3 ± 0.4	41.6 ± 0.4	15.7 ± 0.03
185.97	41.6 ± 0.3	42.1 ± 0.4	15.6 ± 0.03
189.42	42.0 ± 0.4	41.5 ± 0.4	15.9 ± 0.03
192.87	41.9 ± 0.4	41.6 ± 0.4	15.8 ± 0.03
196.32	42.0 ± 0.4	41.9 ± 0.4	16.1 ± 0.03
199.77	42.4 ± 0.4	41.4 ± 0.3	16.0 ± 0.03
203.22	42.9 ± 0.4	41.4 ± 0.3	16.1 ± 0.03

Dose (10^{15} ions cm^{-2})	Ag composition	In composition	Yb composition
206.67	41.9 ± 0.4	41.7 ± 0.3	15.9 ± 0.03
210.12	42.1 ± 0.4	42.3 ± 0.4	16.0 ± 0.03
213.57	43.2 ± 0.4	41.6 ± 0.4	16.0 ± 0.03
217.03	42.7 ± 0.4	41.1 ± 0.3	16.0 ± 0.03
220.48	41.6 ± 0.3	42.3 ± 0.4	15.8 ± 0.03
223.93	42.7 ± 0.4	41.4 ± 0.4	16.0 ± 0.03
227.38	42.5 ± 0.4	41.5 ± 0.3	16.1 ± 0.03
230.83	42.1 ± 0.4	42.0 ± 0.4	16.0 ± 0.03
234.28	41.9 ± 0.4	42.3 ± 0.4	15.8 ± 0.03
237.73	42.2 ± 0.4	41.8 ± 0.4	16.3 ± 0.03
241.18	42.8 ± 0.4	42.1 ± 0.4	15.8 ± 0.03
244.63	42.7 ± 0.4	41.7 ± 0.3	16.0 ± 0.03
248.08	43.1 ± 0.4	41.7 ± 0.3	16.0 ± 0.03
251.54	42.0 ± 0.2	42.0 ± 0.2	16.0 ± 0.02
254.99	42.0 ± 0.2	42.0 ± 0.2	16.0 ± 0.02
258.44	42.0 ± 0.2	42.0 ± 0.2	16.0 ± 0.02

Table 8: Table listing LEIS composition change with dose applied for sputtering round 3.

Dose (10^{15} ions cm^{-2})	Ag composition	In composition	Yb composition
0.38	27.72 ± 0.03	56.65 ± 0.2	16.466 ± 0.006
0.77	30.8 ± 0.3	58.5 ± 0.2	16.534 ± 0.005
1.92	38.1 ± 0.3	59.2 ± 0.2	15.407 ± 0.005
3.07	42.5 ± 0.3	58.0 ± 0.2	14.289 ± 0.004
4.22	44.5 ± 0.3	55.9 ± 0.2	14.168 ± 0.004
5.37	44.3 ± 0.3	54.6 ± 0.2	14.036 ± 0.005
6.52	45.6 ± 0.3	53.5 ± 0.2	13.773 ± 0.005
7.67	46.5 ± 0.3	52.2 ± 0.2	13.940 ± 0.005
8.82	47.1 ± 0.3	51.2 ± 0.2	13.612 ± 0.005
9.97	47.3 ± 0.3	50.2 ± 0.2	13.489 ± 0.005
11.12	47.4 ± 0.3	49.6 ± 0.2	13.632 ± 0.005
12.27	48.3 ± 0.3	49.2 ± 0.2	13.511 ± 0.005
13.42	48.7 ± 0.3	48.4 ± 0.2	13.520 ± 0.005
14.57	49.1 ± 0.3	47.7 ± 0.2	13.467 ± 0.005
15.72	48.8 ± 0.3	47.8 ± 0.2	13.441 ± 0.005
16.87	49.9 ± 0.3	47.1 ± 0.2	13.079 ± 0.005
18.02	50.2 ± 0.3	46.9 ± 0.2	13.136 ± 0.005

Dose (10^{15} ions cm^{-2})	Ag composition	In composition	Yb composition
19.17	50.2 ± 0.3	46.3 ± 0.2	13.048 ± 0.005
20.32	50.5 ± 0.3	45.9 ± 0.2	13.090 ± 0.005
21.47	50.5 ± 0.3	45.5 ± 0.2	12.927 ± 0.005
22.62	51.0 ± 0.3	45.4 ± 0.2	12.819 ± 0.005
23.77	51.0 ± 0.3	44.8 ± 0.2	12.896 ± 0.005
26.07	53.4 ± 0.3	44.8 ± 0.2	12.648 ± 0.005
28.37	52.7 ± 0.2	44.1 ± 0.2	12.696 ± 0.005
30.68	52.6 ± 0.3	44.2 ± 0.2	12.833 ± 0.005
32.98	52.2 ± 0.3	44.0 ± 0.2	12.927 ± 0.005
35.28	52.4 ± 0.3	43.9 ± 0.2	12.762 ± 0.005
37.58	51.8 ± 0.3	44.5 ± 0.2	12.83 ± 0.005
39.88	52.1 ± 0.3	44.4 ± 0.2	12.956 ± 0.005
42.18	51.5 ± 0.3	44.7 ± 0.2	12.962 ± 0.005
44.48	51.4 ± 0.3	44.3 ± 0.2	13.017 ± 0.005
46.78	50.7 ± 0.2	44.7 ± 0.2	13.050 ± 0.005
49.08	51.0 ± 0.3	44.3 ± 0.2	13.215 ± 0.005
51.38	50.4 ± 0.3	44.2 ± 0.2	13.311 ± 0.005
53.68	50.8 ± 0.3	44.1 ± 0.2	13.129 ± 0.005
55.98	50.5 ± 0.3	44.0 ± 0.2	13.527 ± 0.006
58.28	50.1 ± 0.3	43.9 ± 0.2	13.478 ± 0.006
60.58	50.3 ± 0.3	43.7 ± 0.2	13.555 ± 0.006
62.88	50.0 ± 0.3	44.0 ± 0.2	13.470 ± 0.006
65.18	49.5 ± 0.3	44.0 ± 0.2	13.709 ± 0.006
67.49	49.6 ± 0.3	43.7 ± 0.2	13.751 ± 0.006
69.79	49.1 ± 0.3	43.6 ± 0.2	13.880 ± 0.006
72.09	48.8 ± 0.3	43.9 ± 0.2	13.841 ± 0.006
74.39	48.5 ± 0.3	43.7 ± 0.2	13.909 ± 0.006
76.69	48.8 ± 0.3	43.8 ± 0.2	14.118 ± 0.006
78.99	48.2 ± 0.3	43.8 ± 0.2	14.109 ± 0.006
81.29	48.7 ± 0.3	43.2 ± 0.2	14.137 ± 0.006
83.59	48.0 ± 0.3	43.4 ± 0.2	14.267 ± 0.006
85.89	47.8 ± 0.3	43.7 ± 0.2	14.304 ± 0.006
88.19	47.5 ± 0.3	43.5 ± 0.2	14.126 ± 0.006
90.49	47.8 ± 0.3	43.3 ± 0.2	13.984 ± 0.006
92.79	46.8 ± 0.2	43.8 ± 0.2	14.306 ± 0.006
95.09	47.5 ± 0.3	43.4 ± 0.2	14.405 ± 0.006
97.39	47.2 ± 0.3	43.4 ± 0.2	14.403 ± 0.006

Dose (10^{15} ions cm^{-2})	Ag composition	In composition	Yb composition
99.69	46.5 ± 0.3	43.7 ± 0.2	14.493 ± 0.006
101.99	46.6 ± 0.3	43.4 ± 0.2	14.596 ± 0.006
104.3	46.6 ± 0.3	43.1 ± 0.2	14.748 ± 0.006
106.6	46.3 ± 0.3	43.2 ± 0.2	14.653 ± 0.006
108.9	46.2 ± 0.3	43.4 ± 0.2	14.656 ± 0.006
111.2	45.8 ± 0.3	43.3 ± 0.2	14.794 ± 0.006
113.5	46.0 ± 0.3	43.1 ± 0.2	14.513 ± 0.006
115.8	45.7 ± 0.3	43.0 ± 0.2	14.803 ± 0.006
118.1	45.6 ± 0.3	43.1 ± 0.2	14.790 ± 0.006
120.4	45.6 ± 0.3	42.6 ± 0.2	14.992 ± 0.006
122.7	45.1 ± 0.3	43.2 ± 0.2	14.845 ± 0.006
125	45.4 ± 0.3	42.8 ± 0.2	14.827 ± 0.006
127.3	45.0 ± 0.3	43.1 ± 0.2	15.115 ± 0.006
129.6	45.0 ± 0.3	42.9 ± 0.2	15.115 ± 0.006
131.9	45.3 ± 0.3	42.8 ± 0.2	14.935 ± 0.006
134.2	44.8 ± 0.3	42.7 ± 0.2	15.073 ± 0.006
136.5	44.4 ± 0.3	43.2 ± 0.2	15.442 ± 0.007
138.8	44.6 ± 0.3	42.8 ± 0.2	14.904 ± 0.006
141.11	44.1 ± 0.3	43.1 ± 0.2	15.137 ± 0.006
143.41	44.0 ± 0.3	42.9 ± 0.2	15.310 ± 0.006
145.71	44.3 ± 0.3	42.6 ± 0.2	15.396 ± 0.006
148.01	44.2 ± 0.3	42.6 ± 0.2	15.301 ± 0.006
150.31	44.3 ± 0.3	42.6 ± 0.2	15.361 ± 0.007
152.61	43.4 ± 0.2	42.9 ± 0.2	15.519 ± 0.007
154.91	43.8 ± 0.3	42.6 ± 0.2	15.282 ± 0.007
157.21	44.1 ± 0.3	42.3 ± 0.2	15.356 ± 0.007
159.51	43.3 ± 0.2	42.9 ± 0.2	15.189 ± 0.007
161.81	43.5 ± 0.3	42.9 ± 0.2	15.457 ± 0.007
164.11	43.1 ± 0.3	42.9 ± 0.2	15.602 ± 0.007
166.41	43.1 ± 0.3	42.8 ± 0.2	15.271 ± 0.006
168.71	43.6 ± 0.3	42.5 ± 0.2	15.477 ± 0.007
171.01	43.7 ± 0.3	42.6 ± 0.2	15.499 ± 0.007
173.31	43.2 ± 0.3	42.2 ± 0.2	15.385 ± 0.007
175.61	43.7 ± 0.3	42.5 ± 0.2	15.565 ± 0.007
177.92	43.2 ± 0.3	42.2 ± 0.2	15.449 ± 0.007
180.22	43.5 ± 0.3	42.2 ± 0.2	15.444 ± 0.007
182.52	43.2 ± 0.3	42.4 ± 0.2	15.651 ± 0.007

Dose (10^{15} ions cm^{-2})	Ag composition	In composition	Yb composition
184.82	43.3 ± 0.3	42.3 ± 0.2	15.877 ± 0.007
187.12	42.7 ± 0.2	42.4 ± 0.2	15.583 ± 0.007
189.42	43.6 ± 0.3	42.4 ± 0.2	15.464 ± 0.007
191.72	43.8 ± 0.3	42.3 ± 0.2	15.561 ± 0.007
194.02	42.7 ± 0.2	42.3 ± 0.2	15.681 ± 0.007
196.32	43.6 ± 0.3	42.2 ± 0.2	15.717 ± 0.007
198.62	42.3 ± 0.2	42.3 ± 0.2	15.651 ± 0.007
200.92	42.4 ± 0.3	42.2 ± 0.2	15.912 ± 0.007
203.22	42.4 ± 0.3	42.2 ± 0.2	15.681 ± 0.007
205.52	42.4 ± 0.3	42.2 ± 0.2	15.750 ± 0.007
207.82	42.4 ± 0.3	42.1 ± 0.2	15.642 ± 0.007
210.12	42.1 ± 0.3	42.2 ± 0.2	15.785 ± 0.007
212.42	42.4 ± 0.3	42.3 ± 0.2	15.822 ± 0.007
214.73	42.4 ± 0.3	42.0 ± 0.2	15.686 ± 0.007
217.03	42.4 ± 0.3	42.1 ± 0.2	15.884 ± 0.007
219.33	42.3 ± 0.3	41.9 ± 0.2	15.868 ± 0.007
221.63	42.7 ± 0.3	42.0 ± 0.2	15.561 ± 0.007
223.93	42.5 ± 0.3	42.3 ± 0.2	15.778 ± 0.007
226.23	42.7 ± 0.3	42.1 ± 0.2	16.00 ± 0.007
228.53	42.7 ± 0.3	42.5 ± 0.2	15.813 ± 0.007
230.83	41.3 ± 0.2	42.5 ± 0.2	15.870 ± 0.007
233.13	42.4 ± 0.3	42.0 ± 0.2	15.732 ± 0.007
235.43	42.1 ± 0.3	42.0 ± 0.2	15.864 ± 0.007
237.73	42.7 ± 0.3	42.2 ± 0.2	15.820 ± 0.007
240.03	43.2 ± 0.3	42.5 ± 0.2	15.982 ± 0.007
242.33	41.9 ± 0.2	41.6 ± 0.2	15.873 ± 0.007
244.63	42.6 ± 0.3	41.9 ± 0.2	15.985 ± 0.007
246.93	42.3 ± 0.3	41.5 ± 0.2	15.866 ± 0.007
249.23	42.4 ± 0.3	42.3 ± 0.2	15.908 ± 0.007
251.54	42.4 ± 0.3	41.9 ± 0.2	15.969 ± 0.007
253.84	41.6 ± 0.2	42.6 ± 0.2	15.853 ± 0.007
256.14	42.6 ± 0.3	42.1 ± 0.2	16.083 ± 0.007
258.44	43.2 ± 0.3	41.6 ± 0.2	15.796 ± 0.007
260.74	41.9 ± 0.2	42.2 ± 0.2	15.794 ± 0.007
263.04	42.5 ± 0.3	41.6 ± 0.2	15.802 ± 0.007
265.34	41.7 ± 0.2	41.8 ± 0.2	15.824 ± 0.007
267.64	42.0 ± 0.3	41.9 ± 0.2	16.145 ± 0.007

Dose (10^{15} ions cm^{-2})	Ag composition	In composition	Yb composition
269.94	42.2 ± 0.3	42.2 ± 0.2	15.923 ± 0.007
272.24	42.4 ± 0.3	42.1 ± 0.2	16.165 ± 0.007
274.54	41.7 ± 0.2	41.8 ± 0.2	15.949 ± 0.007
276.84	41.9 ± 0.3	42.3 ± 0.2	15.978 ± 0.007
279.14	42.6 ± 0.3	41.9 ± 0.2	15.899 ± 0.007
281.44	41.5 ± 0.2	42.1 ± 0.2	16.024 ± 0.007
283.74	42.2 ± 0.3	42.2 ± 0.2	15.917 ± 0.007
286.04	42.2 ± 0.3	42.1 ± 0.2	16.037 ± 0.007
288.35	42.4 ± 0.3	41.9 ± 0.2	15.938 ± 0.007
290.65	41.3 ± 0.2	41.9 ± 0.2	15.980 ± 0.007
292.95	42.7 ± 0.3	41.9 ± 0.2	15.925 ± 0.007
295.25	42.5 ± 0.3	41.9 ± 0.2	16.053 ± 0.007
297.55	42.2 ± 0.3	41.8 ± 0.2	16.092 ± 0.007
299.85	41.9 ± 0.3	41.9 ± 0.2	15.732 ± 0.007
302.15	41.2 ± 0.2	42.3 ± 0.2	15.943 ± 0.007
304.45	40.7 ± 0.2	42.0 ± 0.2	16.040 ± 0.007
306.75	40.8 ± 0.3	41.9 ± 0.2	15.943 ± 0.007
309.05	41.7 ± 0.3	42.5 ± 0.2	15.956 ± 0.007
311.35	42.4 ± 0.3	41.8 ± 0.2	15.824 ± 0.007
313.65	41.6 ± 0.2	41.4 ± 0.2	15.829 ± 0.007
315.95	40.8 ± 0.2	41.8 ± 0.2	15.954 ± 0.007
318.25	41.4 ± 0.3	41.7 ± 0.2	16.064 ± 0.007
320.55	42.6 ± 0.3	41.9 ± 0.2	16.141 ± 0.007
322.85	42.3 ± 0.3	41.8 ± 0.2	16.051 ± 0.007
325.16	41.6 ± 0.2	41.6 ± 0.2	16.160 ± 0.007
327.46	40.9 ± 0.2	41.7 ± 0.2	15.969 ± 0.007
329.76	41.1 ± 0.3	42.1 ± 0.2	16.079 ± 0.007
332.06	42.7 ± 0.3	41.8 ± 0.2	15.974 ± 0.007
334.36	41.3 ± 0.2	41.9 ± 0.2	15.991 ± 0.007
336.66	40.4 ± 0.2	41.8 ± 0.2	15.561 ± 0.007
338.96	42.1 ± 0.3	41.6 ± 0.2	15.741 ± 0.007
341.26	41.7 ± 0.3	42.2 ± 0.2	15.794 ± 0.007
343.56	42.6 ± 0.3	41.6 ± 0.2	15.952 ± 0.007
345.86	41.5 ± 0.2	41.7 ± 0.2	15.978 ± 0.007
348.16	42.1 ± 0.3	41.3 ± 0.2	16.015 ± 0.007
350.46	41.8 ± 0.3	42.0 ± 0.2	15.985 ± 0.007
352.76	42.1 ± 0.3	41.4 ± 0.2	16.024 ± 0.007

Dose (10^{15} ions cm^{-2})	Ag composition	In composition	Yb composition
355.06	42.0 ± 0.3	41.9 ± 0.2	15.930 ± 0.007
357.36	41.5 ± 0.2	42.1 ± 0.2	16.066 ± 0.007
359.66	42.3 ± 0.3	41.1 ± 0.2	15.980 ± 0.007
361.97	40.7 ± 0.2	41.4 ± 0.2	15.960 ± 0.007
364.27	41.7 ± 0.3	41.5 ± 0.2	15.943 ± 0.007
366.57	42.1 ± 0.3	41.7 ± 0.2	16.279 ± 0.007
368.87	40.6 ± 0.2	41.8 ± 0.2	15.914 ± 0.007
371.17	42.1 ± 0.3	41.0 ± 0.2	15.969 ± 0.007
373.47	42.0 ± 0.3	41.0 ± 0.2	16.022 ± 0.007
375.77	41.7 ± 0.3	41.8 ± 0.2	16.169 ± 0.007
378.07	41.2 ± 0.3	41.7 ± 0.2	16.119 ± 0.007
380.37	40.8 ± 0.3	41.4 ± 0.2	16.088 ± 0.007
382.67	42.0 ± 0.3	41.7 ± 0.2	16.033 ± 0.007
384.97	42.3 ± 0.3	42.0 ± 0.2	16.020 ± 0.007
387.27	42.0 ± 0.3	42.0 ± 0.2	16.000 ± 0.007

7.5.3 Additional C2 Composition

A table showing the C2 plane composition and relation to the LEIS surface composition is given below. These values were derived using the slab model described in the results section.

Species	LEIS Peak Composition	C2 Composition
In	59.28 ± 0.02	55.56
Ag	38.07 ± 0.03	29.62
Yb	15.99 ± 0.02	14.81

Table 9: Table showing C2 composition match compared to the LEIS data. Deviation is explained through high LEIS uncertainty.

7.6 Appendix D - Computational STM Model and Code Repository

7.6.1 Code Repository

The link for all the code used in this project is provided here to allow analysis and future editing:

https://github.com/reght555/Master-Thesis-Code

This includes the fitting software and slab sampling codes mentioned alongside the STM model code.

7.6.2 Brief Model Overview

As previously mentioned, the model used for our STM simulation was the Tersoff-Hamann model. Consequently, a brief overview of the physics behind this model will be presented here.

The Tersoff-Hamann model is obtained from the Bardeen formalism by assuming the tip can be modelled as a spherical potential well. This effectively means that the tip is only contributing s orbital states to the tunnelling current. Using this modification, we may expand the wave states of tip as spherical Bessel functions of the second kind. Substituting this into the matrix tunnelling element equation at low bias voltages we get:

$$M_{\mu\nu} = \frac{\hbar^2}{2m} \int (\psi_s^* \nabla \psi_t - \psi_t^* \nabla \psi_s) \cdot dS \propto |\psi_s| \tag{16}$$

Where ψ_s is the sample wavefunction, ψ_t is the tip wavefunction and $M_{\mu\nu}$ is our matrix element. Substituting this into the tunnelling current equation we find:

$$I \propto \sum |\psi_s|^2 \delta(E_\nu - E_f) \tag{17}$$

Where I is the tunnelling current, E_ν is the state energy level, and E_f is the Fermi energy [67]. The core simplification is, therefore, that we may discount the effects of tip geometry when modelling STM given the tip contribution is simply proportional to that of the sample density of states. Propagating this through we get that the tunnelling current can be expressed as:

$$I \propto e^{-\kappa(dz)} \tag{18}$$

Where dz is our tip distance, and κ is a coefficient related to the surface work-function. If we model the tip as spherically symmetric our dz will be of the form:

$$dz = \frac{(r)^2}{2R} \tag{19}$$

Where r is our displacement and R is our tip radius [68]. This is notably very similar to the displacement parameter used in wave physics to describe spherical waves [69].

We can, therefore, finally express our tunnelling current as proportional to a 2d Gaussian with parameters linked to the species present at the surface (surface electron density).

7.6.3 Model Implementation

The 2d gaussian model was fairly simple to implement taking the following form:

$$I = Se^{-br^2} \tag{20}$$

We added a spatial decay feature linked to the size of the atom (b). This was worked out from the covalent radius of the species present. Yb has a rough covalent radius of 187 pm ,

silver has a radius of 144 pm, and indium has a radius of approximately 167 pm [70]. We took the ratio of these giving a simplest ratio of approximately 8:7:6. These weightings were added to the model by simply adjusting the decay parameter of the Gaussian (b).

Additionally, a bias feature was implemented to roughly approximate the bias dependent contribution of species. We expected Yb to contribute most to the current for our positive bias due to the presence of its 4f shell. Hence, the exponential weighting coefficient (S) was increased for Yb relative to silver and Indium with the ratio (2:1:1).

An exponential height decay feature was also added such that the signal contribution decays with distance. This took the form:

$$A = e^{-\kappa(z)} \tag{21}$$

where (A) is our height decay prefactor, and κ is a decay constant whose value can be changed. This allowed us to model convolution effects from lower planes which was central for confirmation of our A/B hypothesis before DFT can provide more rigorous evidence.

7.6.4 Model Limitations

As it stands, our model is more a reference than able to be used for actual model determination. This is because it contains several severe limitations. That being said building a true STM model would be the equivalent of performing DFT on top of modelling very precise tip geometry which is far beyond the scope of this project. Hence, a simple overview of the model limitations is presented to inform the reader.

Our principal limitation is the lack of tip contribution modelling. Our tungsten tip does not simply contribute s orbital states to the tunnelling current. As mentioned previously, our W tip majority contribution is that of the (d_{z^2}) shell. Hence the Tersoff-Hamann approximation is inherently inaccurate for precise W-tip STM modelling. If we use the Chen model to model tip orbital contributions using derivatives of the wave function, we do find the exponential model is still present. The principal change being that the contribution to the LDOS from each orbital is given by weighted Gaussians with the total contribution being their sum [91]. Consequently, we may assume our model provides some insight with the understanding that specific spreads and 'brightnesses' may change with tip convolution effects fully taken into account. Using weighted Gaussians would be an achievable modification to the model and, we would recommend its inclusion if more time is dedicated to the project later.

A further limitation is our individual treatment of LDOS contributions. Electron densities are not localised to within the covalent radius. Electrons are in fact widely distributed and shared between species. Hence the bias and weighting system used is quite inaccurate. We

capture the essence being that electron density should be highest at the atom locations but, do miss sometimes substantial effects from covalent bonding. Correcting this would require DFT hence, is unachievable for such a short term project.

Furthermore, another limitation to the model is our use of the theoretical bulk. As mentioned in section 2, surfaces relax and reconstruct upon cleavage. Hence, it is likely that, if large scale reconstruction occurs, our bulk model is incorrect. Correction of this error, would be impossible without knowing the surface structure beforehand. It does however, mean that false positive identification of motifs could have occurred where reconstructed regions resemble other regions of the bulk. This represents a major source of uncertainty throughout the entire experimental procedure and is only accounted for by analysis of the raw STM data for anomalies.

7.6.5 Additional Data

A small collection of used simulations and matches is provided below to help supplement the figures provided within the results section:

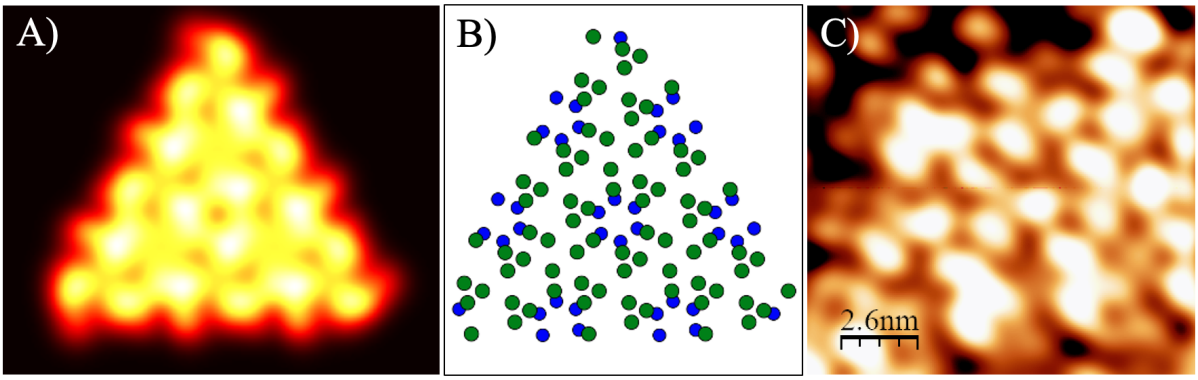


Figure 34: A) Shows a computer simulation of C2 plane section showing mixture of tight irregular triangles and diffuse spiral. B) Is a rendition of the 2D plane with Yb atoms in green, In atoms in blue. C) STM image showing similar motifs to those seen in simulation.

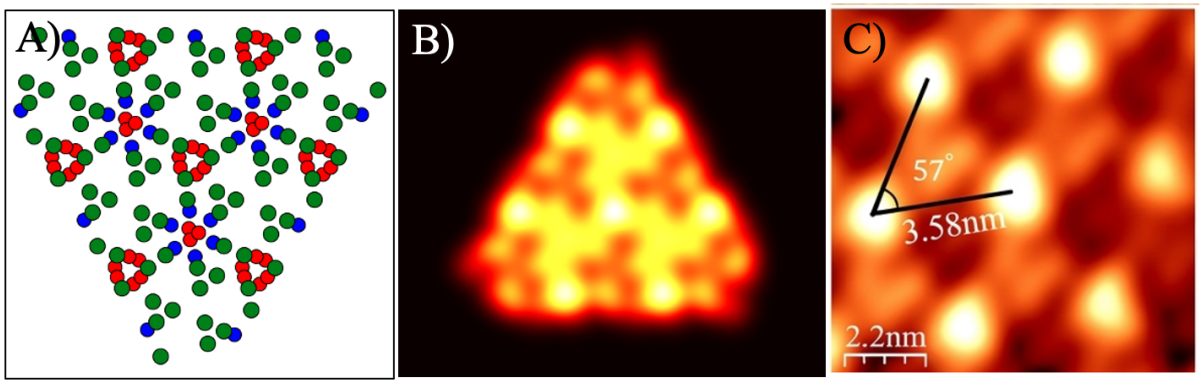


Figure 35: A) A 2D simulation of C2 plane with Ag in red, In in blue and Yb in green. B) Shows a computer simulation of C2 from higher dz point. This time the simulation shows the top regular triangles which shadow the triangles seen in figure (32). C) Matching STM motif with similar size to expression of upper C2 plane under simulation.

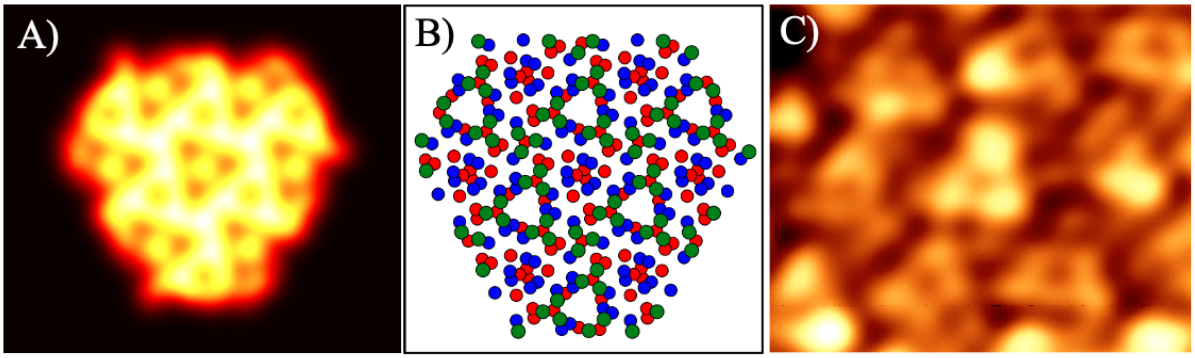


Figure 36: A) A computer simulation of A2 plane showing array of uniform triangles composed of 3 smaller triangles B) A 2D simulation of A2 plane with Ag in red, In in blue and Yb in green. C) Similar triangle motifs with 3 component triangles matching those seen in the simulation.

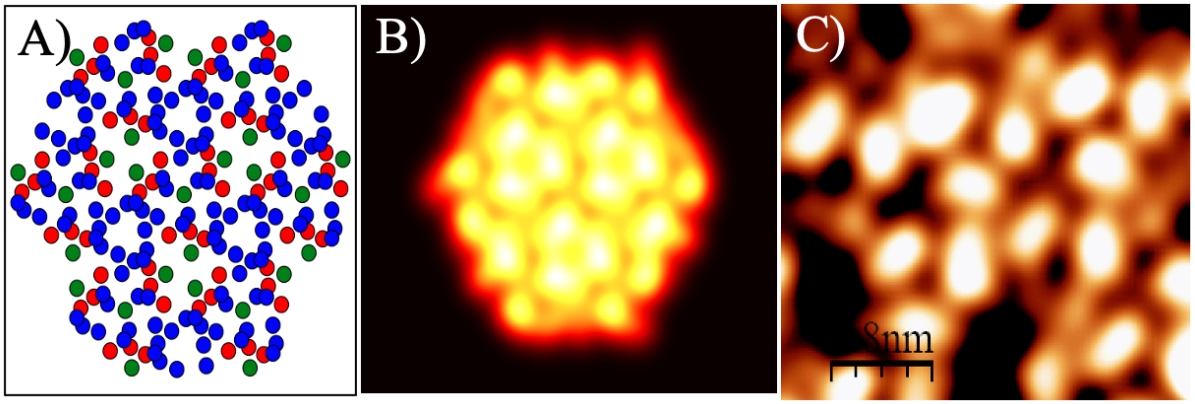


Figure 37: A) A 2D simulation of C3 plane with Ag in red, In in blue and Yb in green. B) A computer simulation of the corresponding C3 plane which demonstrates tight irregular triangles in a periodic array. C) A similar array of tight irregular triangles seen in STM image. The LDOS is slightly more diffuse than our model likely due to hybridisation of electron densities between closely packed atom arrangements.

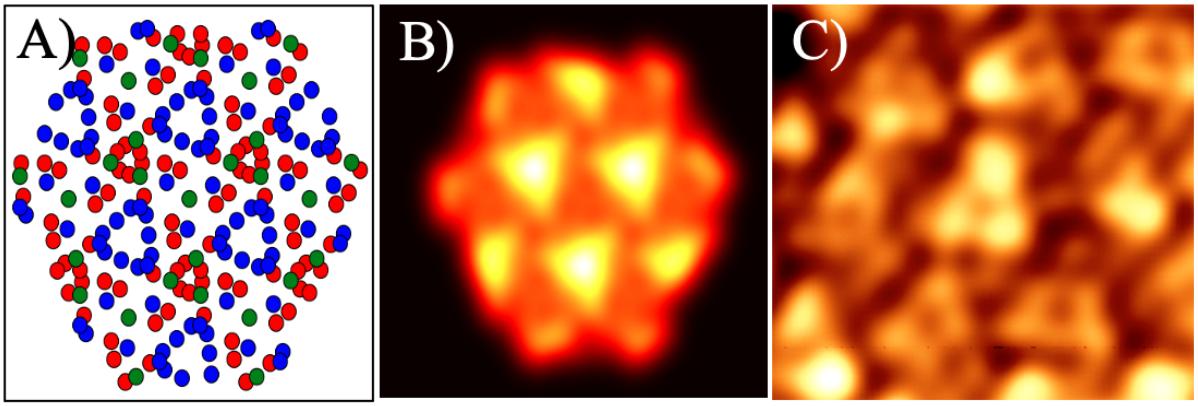


Figure 38: A) A 2D simulation of C1 plane with Ag in red, In in blue and Yb in green. B) Computer simulation of C1 plane showing uniform triangles. C) STM image showing similar patterns. Our model slightly overestimates LDOS contribution which may explain why smaller triangle composition isn't identified.

7.7 Appendix E - VESTA Analysis

Due to spatial constraints, the exact use of Vesta has remained quite vague throughout the main report body. This appendix aims to briefly describe an example of Vesta use and matching procedure, as well as, provide some extra data in support of the results section.

7.7.1 Analysis an Example

For our example we will show the isolation of the C2 plane and demonstrate overlay onto the cleaned data image M10.

First, we import our theoretical bulk coordinates and open them in Vesta. This displays a one unit cell model of the theoretical bulk. To perform proper plane analysis we require a much larger structure. Hence, we adjust the boundaries from 0-1 to 0-3. This creates a 3x3 block of unit cells predicting the atomic positions using the inherent structure symmetry read from our coordinate file.

Next, we rotate the structure such that the (111) vector is pointing directly into the screen ie we are looking along the (111) direction. Then, a simple 90^o rotation is performed, aligning the (111) axis with our z axis allowing us to identify plane progressions.

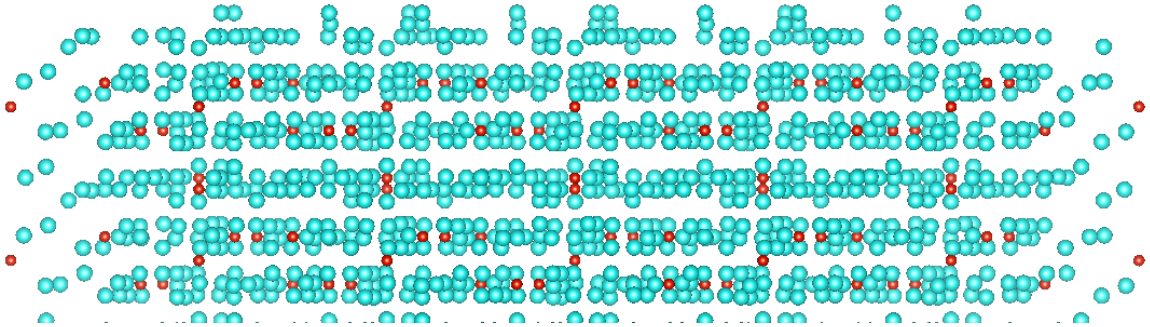


Figure 39: Vesta image showing planes with 111 vector direction pointing up page plane. In the image only Yb atoms are shown (turquoise) and cluster centres (red). This was done for clarity purposes.

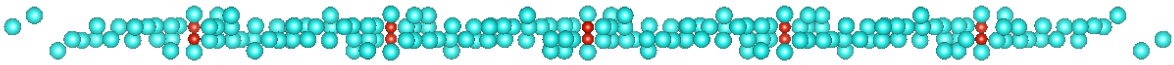


Figure 40: Isolated Vesta image of C plane with 4 subplanes shown. In the image only Yb atoms are shown (turquoise) and cluster centres (red). This was done for clarity purposes.

Due to the number of atoms present, we initially remove In and Ag atoms allowing us to identify the clear Yb subplanes. Using our knowledge of the theoretical structure we can then identify the C planes present in the structure. These contain 4 sub planes and are relatively unique. For the mirrored A and B planes we use our progression A to B to C to identify them using the nearest C plane as a reference.

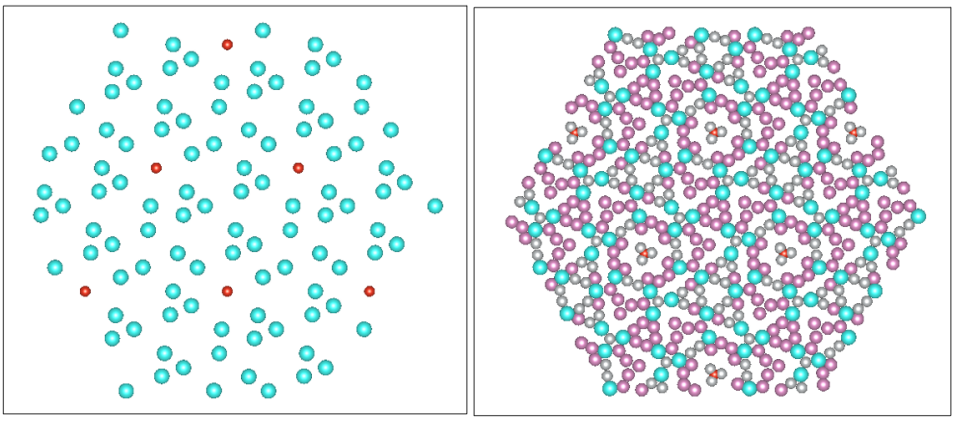


Figure 41: Left hand image is a Vesta image of C2 plane only showing Yb (blue) and cluster centres (red). Right hand image is the same C2 plane but now including In (purple) and Ag (silver). We can see very dense arrays of triangles in the right hand image.

We then isolate C2, by selecting and deleting all other Yb atoms. This gives us a view of the C2 plane alone. After another 90^o rotation, we obtain an image of our theoretical plane looking down along the (111) axis. An image is then taken of this Yb only C2 plane for use within overlay analysis. Then adding back in our In and Ag atoms and, isolating only the atoms present within the C2 subplane another image is taken to show the Ag-In containing C2 plane.

Finally, for the overlay process, our two plane images are fed into AI to remove the white Vesta background. The edited images are then imported into Inkscape. In Inkscape we then add polygons over the atomic motifs to show what they may appear blurred under low STM resolution. The scale of these polygons is adjusted manually and calibrated using the known Vesta motif sizes as a scaling reference.

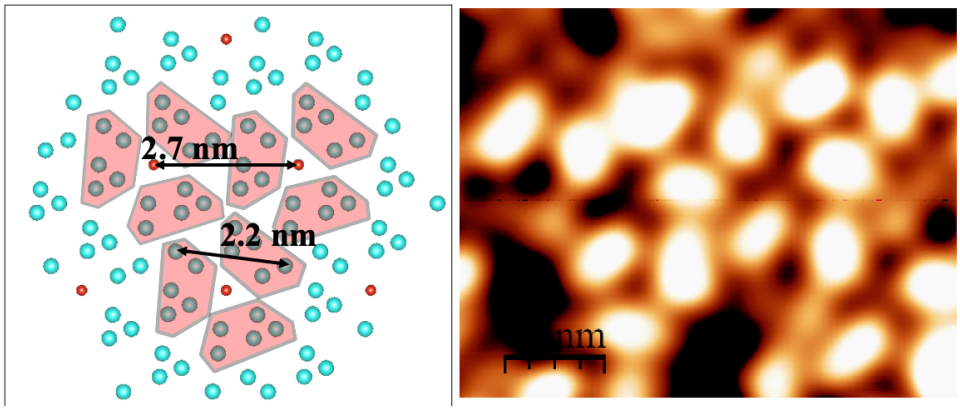


Figure 42: Left hand image is Vesta image with rough overlay of motif polyhedra. We can see that the Yb only LDOS consists of large irregular triangles. The right hand image shows a possible match to the Yb only fit with similar tight irregular triangles in array.

The image can then be imported into a separate Inkscape file containing the cleaned STM

image. We finely adjust the size of our image using a reference Vesta measurement and matching this with the inbuilt scale within the STM image. The correctly scaled image is then overlayed over the raw STM image to allow identification of visual matches. An example of our C2 plane next to M10 is given below:

We repeated this example process for all the sub planes and raw STM images which in turn allowed us to construct our sub plane model.

7.7.2 Motif Measurements

We made atomic measurements by highlighting our one desired atom at the edge of the motif and noting down its coordinates. Then we repeated the same procedure for the atom at the opposite end of our desired motif. We then multiplied the coordinates by the following (111) basis conversion matrix:

$$M = \begin{bmatrix} \frac{1}{\sqrt{2}} & -\frac{1}{\sqrt{2}} & 0 \\ \frac{1}{\sqrt{6}} & \frac{1}{\sqrt{6}} & -\frac{2}{\sqrt{6}} \\ \frac{1}{\sqrt{3}} & \frac{1}{\sqrt{3}} & \frac{1}{\sqrt{3}} \end{bmatrix} \tag{22}$$

This allowed us to calculate the distance using the first two components of our converted vectors. This is done simply using the standard euclidean metric formula.

7.8 Appendix F - Required Materials

7.8.1 AI summary

AI was consulted during the course of this project to remove the white background from Vesta images. Additionally, Grammarly, an AI based grammar tool, was used to check for typos when writing parts of this thesis.

7.8.2 Copy of Project Plan

7.8.3 Introduction

Quasicrystals are crystals showing aperiodic order, which is to say having no directly repeating structure. This is in stark contrast to regular crystallography, where the crystallographic restriction theorem [1] limits the possible crystal structures to 14 separate periodic Bravais lattices. As a consequence of this aperiodic order, quasicrystals demonstrate many scientifically interesting properties, including novel adsorption behaviour and 'forbidden' symmetry [2].

The main difficulty in studying quasicrystals is this aperiodic structure making determination of

their surface structure extraordinarily challenging. A pertinent solution to this problem presents itself through the use of Quasicrystal approximants. These locally approximate the QC structure but have a periodic structure [3]. Approximants thus provide a way to study composite elements of the QC structure without the issues that arise from aperiodicity.

Within this project we focus on the 2/1 Ag-In-Yb approximant with the main aim of determining its surface structure and chemistry. This will then be used to explore and explain any deviations from the theoretical predictions given by Density functional Theory calculations. Results of this analysis may then form part of a possible paper on the structure.

7.8.4 Methods

Several Methods are commonly used to determine surface structure and chemistry. The two that this project employs are Low Energy Ion Spectroscopy and Scanning Tunnelling Microscopy.

STM uses the Quantum tunnelling effect to measure the location of atoms on the surface. Explicitly, a bias voltage is applied to the sample, a scanning tip is then placed a set distance (¡1nm) above the surface. The tunnelling current of e^- tunnelling across the vacuum gap into the tip is then measured. This tunnelling current decays exponentially with separation distance between the tip and the atomic surface. By uniformly scanning the surface and measuring the current change, a model of the various density of states of the surface atoms can be interpolated. This provides us with a reflection of the overall surface topography [4].

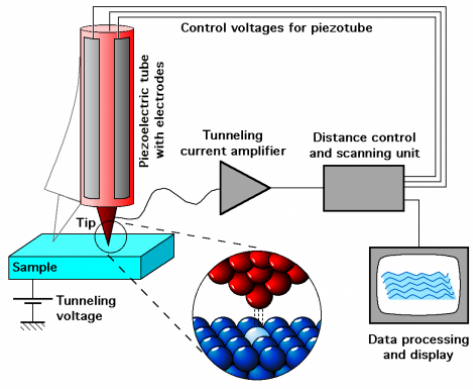


Figure 43: Apparatus used for STM analysis

LEIS, meanwhile, uses ions fired at a specific known kinetic Energy E_k towards the surface. The ions scatter off the surface with a specific energy E_f which is proportional to both the scattering angle ν and the atomic mass of the scattering atom. A plot of the relative frequency of ions scattered vs measured ion energies can then be made, which represents the frequency of atomic species within the surface layer [5]. This data combined with STM data of the surface,

and knowledge of the bulk crystal structure can be used to completely derive the surface atomic structure.

7.8.5 Planned Work

STM data for the 2/1 approximant has already partially been obtained by Dr Coates. My initial project will focus on analysis of this data using the program WSxM. WSxM can be used to derive the various terrace heights and atom cluster locations on the surface. Once this data is compiled and organised, determination of the approximant structure can be made. This will be achieved by comparison of the STM height and position data with the known bulk structure visualised using Vesta. Further STM images will need to be taken to confirm any findings. These shall be completed by myself or Dr Coates within the STM lab from week 4 onwards. Overall, this work will be very similar to work undertaken in [6] on the 1/1 approximant. Hence, the paper can/will be used as a rough guide as to how far work has progressed on the sample. This data analysis process will be expected to comprise the majority of work for weeks 3 through 9.

After compiling the data, work will be undertaken to explain the various motifs found. For instance, the physics behind the specific terrace formation locations. Data on the change in surface composition after sputtering and annealing at various temperatures will also need to be taken to derive the change in surface chemistry after sample processing. This will be completed using LEIS or possibly XPS. This will likely be a continuous process starting after the initial data is analysed by the end of week 4.

Additional work will be completed using LEIS to determine the chemical composition of the surface layer. Work will take place within the Engineering labs with the complete timetable yet to be completely finalised. It is expected that LEIS of the sample shouldn't take more than a week with data analysis and error calculation then also expected to be completed by the end of the following week.

A Gantt chart of the schedule of work is found below in Figure 3 with the work culminating in a complete experimental picture of both the surface structure and chemistry of 2/1 Ag-In-Yb approximant, as well as, an explanation for any deviations seen between the DFT predicted theoretical structure and the real surface observed. Additionally, the write-up timelines are also included in the Gantt chart along with their respective deadlines.

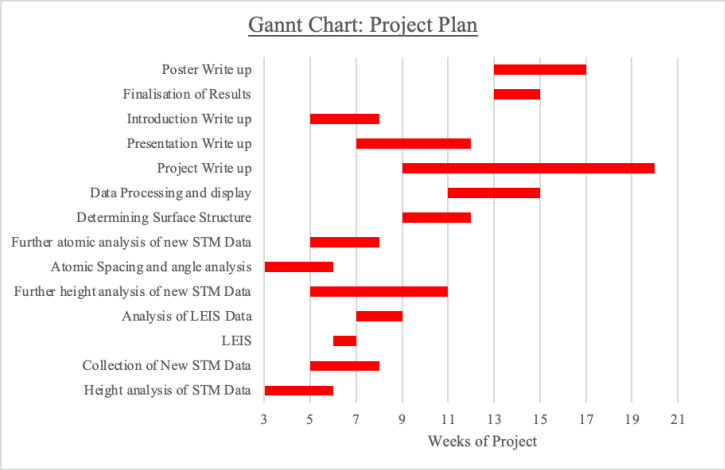


Figure 44: Gantt chart showing planned schedule of work, analysis and write-up

Work plans are subject to change, specifically in regards to the LEIS data acquisition. Given the LEIS equipment requires collaboration with the engineering department availability of the equipment may be subject to unseen constraints. Any updates in the schedule of work will be found and explained within the relevant logbook sections.

7.8.6 References

[1] John Bamberg, Grant Cairns, Devin Kilminster, The Crystallographic Restriction, Permutations, and Goldbach's Conjecture, American Mathematical Monthly, 2003

[2] Sam Coates, Quasicrystal systems with simple symmetries pg(1), The University of Liverpool, 2019

[3] Sam Coates, Quasicrystal systems with simple symmetries pg(16), The University of Liverpool, 2019

[4] Surface Science Lecture Notes 4, Hem Raj Sharma, The University of Liverpool

[5] Stanislav Prusa, Matthew R Linford, A practical guide to interpreting low energy ion scattering (LEIS) spectra, Applied Surface Science volume 657, 2024

[6] Kai M Oliver, Surface Analysis of the Ag-In-Yb 1/1 Quasicrystal Approximant, MSc Project Liverpool University, 2011

[7] Sam Coates, Ronan Mcgrath, Hem Raj Sharma, Influence of differences in orientational planar density on the growth of Pb on the i-Ag–In–Yb quasicrystal, American journal of Physics, 2019

7.8.7 Lay Summary

Surfaces Science represents some of the most complex and cutting edge physics out there. It covers diverse topics from abstract mathematics to complicated experimental procedures. Surfaces are far from as simple as they appear with the naked eye. Instead of smooth surfaces, our world

is rough and chaotic on the microscopic scale. Although, often these surfaces look horrendously complicated we can actually identify clear patterns and structure within them. We can then use these patterns to create catalysts and other exciting chemical technologies.

One of the most interesting examples of these complicated but simultaneously simple surfaces, is known as a quasicrystal. These are literally almost (quasi) - crystals. Now scientists are very picky about what they call crystals. In fact, to be known as a crystal, a solid has to be periodic ie it repeats like a pattern. What makes quasicrystals so interesting is that they don't demonstrate this repeating structure. That may sound strange but, one really simple way to visualise this is with kitchen tiles. Take a flat kitchen floor and try and cover it completely with pentagonal tile. What you find is that it doesn't work there's no way to completely tile the floor without gaps. This is in fact a famous example of an aperiodic pattern known the Penrose tiling. Quasicrystals are exactly like these poorly fitting tiles but in 3 dimensions.

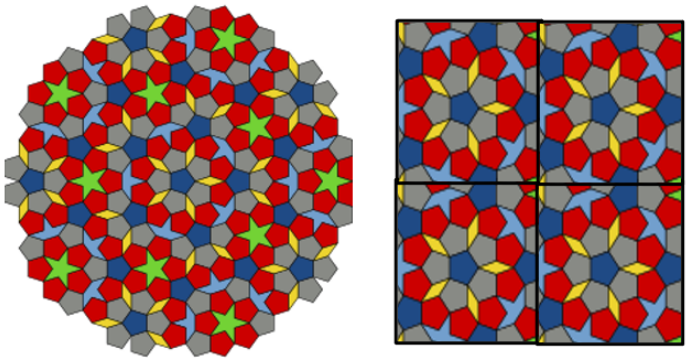


Figure 45: Example of Penrose tiling on the left next to approximant to that tiling on the right.

Just like these tile patterns quasicrystals themselves are very complicated. However, just like with tiles we can take a square cut out of the pattern and create a perfect tiling. This is an approximation to the quasicrystal sharing some of its structure but repeating throughout space like a regular crystal. These are much easier to study but still provide invaluable insight into how quasicrystals behave on a chemical level. Hence, by understanding the surface of these approximants we can better understand the much more complicated quasicrystal. So how do we look at surfaces? Its an interesting question with lots of very famous, Nobel prize winning answers. We use one particular method known as scanning tunnelling microscopy (STM). To understand how this works, we need to understand a bit of quantum mechanics. A bit daunting at first but nothing to worry about I assure you. Effectively our world is made up of atoms, these atoms are surrounded by a sea of electrons existing in many different 'places' (states). These states can sometimes tunnel ie jump from one place to another. This may seem ridiculous but its been proven since the 1920s and is the basis of much of the technology you use daily, as well

as, the main mechanism through which our sun first ignited. Putting all of this together STM uses these tunnelling electrons to build a picture of the sea of electrons of our sample. We see an image with areas with lots of electrons (states) shown as bright region and few electrons shown as dark spots. This very roughly maps to the location of atoms in our sample. Consequently, STM gives us a rough idea of what the surface looks like at the atomic scale.

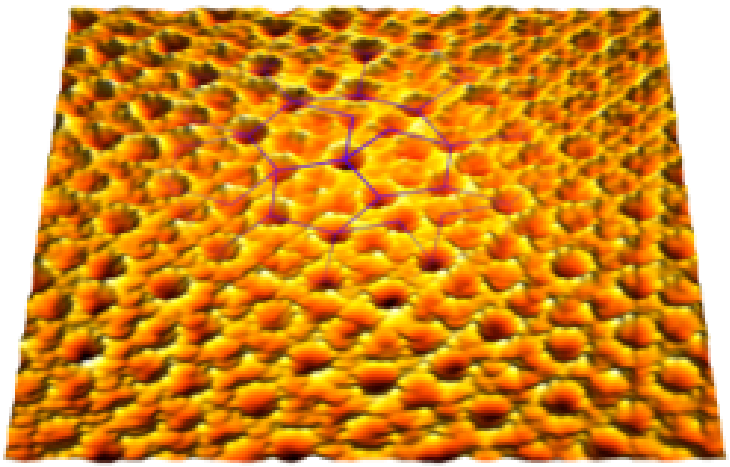


Figure 46: Example of STM image showing structure of lead surface.

In our study we used STM on a Silver- Ytterbium -Indium approximant whose structure had never been studied before. We did this along a very specific angle known as the (111) direction. From our STM studies we identified lots of groups (motifs) of atoms on the surface and used these to build a model of the surface. Using our model we were able then to suggest which of the possible surfaces were more common ie more stable. To explain this a bit more clearly: surfaces want to minimise the amount of energy they have. Consequently, they try to form along more stable less energetic planes. Hence, the most common surfaces that we see are very likely to be the most stable. Therefore, by imaging the surface using STM we can predict the stability of the different layers of the approximant structure by seeing which ones show up at the surface.

We also used another technique known as Low energy ion spectroscopy. This works by literally firing ions at the surface of our sample and measuring their energy when they reflect off atoms on our sample surface. Depending on the atom the ions reflected off of they transfer a certain amount of energy. Therefore, if we measure the ion energy before and after collision, we can work out what atom they've bounced off. If we do this many thousands of times we can see roughly how common certain atoms are based on the number of ions they deflect. More common atoms cover more of the sample so have a higher probability to reflect an incoming ion.

Using Leis we were consequently able to build a picture of our actual surface composition. STM only shows electrons not the type of atom to which they belong. Hence, if we use LEIS

alongside STM, we can build up an idea of both the surface structure, composition and chemistry. This is effectively what we did during this study building a comprehensive understanding of the surface and its formation. This should hopefully allow development of novel materials and encourage further study into approximants.

7.8.8 Overview of Contributions from others

Throughout the work many contributions were primarily provided by others. I have provided here an overview of what work was contributed:

Dr Coates provided the STM model code base including all the imaging features present within the current simulation. My contribution to the code was to change the way the structure was sliced. This allowed me to specify a certain z coordinate, a viewing direction, number of planes and dz thickness. All other code used was my own and was written by myself. Dr Coates also collected the STM images used for analysis with my contribution being the analysis and interpretation of this STM data. As a result, the STM methodology section reflects this in not specifying the STM procedure used only the analysis methods.

Dr Gardner ran the LEIS experiments alongside myself doing the majority of the lab work due to the technical nature of the work and the fact I was crutches at the time. The initial analysis including providing the raw integrated counts was also completed under his supervision and with his help.

Throughout the process a significant number of ideas about image convolution and structure have been provided by Dr Sharma.